

c. 1

INVERSION OF MAGNETOTELLURIC IMPEDANCES
FROM ABOVE YOUNG LITHOSPHERE

by

KENNETH PATRICK WHITTALL

B.Sc., The University of British Columbia, 1977

A THESIS SUBMITTED IN PARTIAL FULFILMENT OF
THE REQUIREMENTS FOR THE DEGREE OF
MASTER OF SCIENCE

in

THE FACULTY OF GRADUATE STUDIES
Department of Geophysics and Astronomy

We accept this thesis as conforming
to the required standard

THE UNIVERSITY OF BRITISH COLUMBIA

October 1982

© Kenneth Patrick Whittall, 1982

In presenting this thesis in partial fulfilment of the requirements for an advanced degree at the University of British Columbia, I agree that the Library shall make it freely available for reference and study. I further agree that permission for extensive copying of this thesis for scholarly purposes may be granted by the head of my department or by his or her representatives. It is understood that copying or publication of this thesis for financial gain shall not be allowed without my written permission.

Department of GEOPHYSICS AND ASTRONOMY

The University of British Columbia
1956 Main Mall
Vancouver, Canada
V6T 1Y3

Date SEPT 30, 1982

Abstract

Ocean bottom magnetometer data from a site on the Pacific plate above 3 my old lithosphere are inverted for electrical conductivity as a function of depth. Magnetotelluric impedances are calculated by the vertical gradient method using the fields at the OBM in conjunction with those measured at the Victoria Geomagnetic Observatory. The approximations involved are examined. Winnowing criteria are proposed which isolate those impedances compatible with all the model and source field assumptions. These then define the best possible data set. A number of inversion algorithms are applied to the data and a wide range of acceptable conductivity profiles are constructed. All profiles exhibit a uniform, relatively high conductivity of about 0.2 S/m from the surface down to a depth of 100 km. Exact and approximate bounds on the conductance are calculated in an effort to quantify the non-uniqueness of the diverse conductivity models. Profiles with a minimum of structure are used to calculate the partial melting and temperature variations beneath the 3 my old site. All results are compared with three other magnetotelluric analyses above 1, 30 and 72 my old lithosphere. The 3 my old datum is discordant and does not fit the trends interpreted from the other three studies.

Table of Contents

Abstract	ii
List of Figures	v
Acknowledgements	vi
Chapter 1 The Ocean Bottom Magnetotelluric Method	1
1.1 Introduction	1
1.2 The Experiment	4
Chapter 2 Theory of the Magnetotelluric Method	12
2.1 MT Fields in a One Dimensional Earth	12
2.2 MT Fields in a Two Dimensional Earth	19
2.3 Derivation of the Impedance Tensor for 1-D Models ...	23
2.4 Impedance Tensor Invariants and Symmetries	26
2.5 Impedances from Magnetic Fields Alone	27
2.6 Plane Wave Assumption	33
2.7 Sphericity of the Earth	35
Chapter 3 Data Reduction	36
3.1 Taking Transforms	36
3.2 Scalar Ratio Estimates	38
3.3 Tensor Ratio Estimates	42
3.4 Winnowing Ratio Estimates	45
3.4.1 Ocean Filter	45
3.4.2 Vertical Field	46
3.4.3 Ratio errors	46
3.4.4 Dispersion Relations and Inequalities	47
3.5 OBM Data Reduction	50
Chapter 4 Inversion of Impedances for Conductivity	54
4.1 Best Fitting Models	56

4.2 Layered Models	56
4.2.1 A Layer over a Halfspace	56
4.2.2 Constant $\mu\sigma h^2$ Layers	57
4.3 Smooth Models	60
4.3.1 Linearized Inversion	60
4.3.2 Gel'fand-Levitan Inversion	61
4.4 Conductance Bounds	61
Chapter 5 Conclusions	66
5.1 OBM Results Compared with Other Studies	66
5.2 Suggestions for Future Work	74
References	78

List of Figures

Figure 1	Experiment location map	6
Figure 2	Four days of OBM data	7
Figure 3	Four days of VIC data	9
Figure 4	Complete OBM horizontal D channel	10
Figure 5	One dimensional model	13
Figure 6	Two dimensional model	20
Figure 7	Ocean filter	31
Figure 8	Winnowing criteria	48
Figure 9	Final apparent resistivities and phases	53
Figure 10	OBM conductivity models	58
Figure 11	OBM conductance bounds	64
Figure 12	Minimum structure conductivity models	67
Figure 13	OBM partial melting and temperature curves	70
Figure 14	JDF, CAL, NCP partial melting and temperature curves	72

Acknowledgements

I thank Dr. Doug Oldenburg for his ebullient support throughout the tenure of this project. His morning chalk talks were as revivifying as a 50 mile bicycle ride and when the dust settled an aphorism or two was usually found. As well, I thank Dr. Lawrie Law for his months of hard work spent in acquiring, and his generosity in supplying, the superb quality magnetometer data. I thank Kerry Stinson, Wang Jia Ying and Don Plenderleith for many interesting discussions and suggestions, the spirits of which are incarnate in this thesis. Thanks are also due all the other people of the department who make work here very pleasant indeed.

CHAPTER 1 THE OCEAN BOTTOM MAGNETOTELLURIC METHOD

1.1 Introduction

Electromagnetic fields are induced in the earth by a variety of natural sources. The worldwide occurrence of lightning storms generates high frequency oscillations greater than about 1 Hz. Below 1 Hz, micropulsations in the earth's magnetic field cause variations over a wide band of periods ranging from 1 to 600 s. At longer periods (minutes to days) magnetic storms resulting from the interaction of the solar wind plasma with the magnetosphere dominate the spectrum. A ring current forms at an altitude of from 2 to 10 earth radii as oppositely charged particles spiral along magnetic field lines in opposite directions. The quiet day solar variation (Sq) derives from a large, stable current system concentrated in the ionosphere near the magnetic poles. This occurs mainly in response to solar heating with perturbations perpetrated by the solar wind. Movements of the highly conducting ocean generate additional fields which are important for this particular ocean bottom experiment. Surface and internal waves, turbulence, tides and currents all contribute to the natural electromagnetic field observed on the ocean floor. Larsen (1973), Filloux (1973) and Cox et al (1970) discuss both ionospheric and oceanic sources and their relevance to electromagnetic induction at sea.

The electromagnetic (EM) waves generated by all sources reflect from and refract into the earth. The refracted waves diffuse vertically downward for almost any angle of incidence because of the high air/earth conductivity contrast. In

general, the earth attenuates short period oscillations more rapidly than long period ones and conductors attenuate the fields more than resistive layers. A measure of the decay as a function of frequency is the magnetotelluric impedance $Z(\omega) = E(\omega)/H(\omega)$ where $E(\omega)$ and $H(\omega)$ are orthogonal frequency domain electric and magnetic fields, respectively (Cagniard, 1953). If, over an isotropic, horizontally layered (one dimensional) earth, the impedance is known precisely at every frequency then the conductivity-depth profile, $\sigma(z)$, is determined exactly (Bailey, 1970). Thus, the variation of penetration of EM waves as coded by $Z(\omega)$ is the key to unlocking the conductivity structure of a one dimensional earth.

Over a more complex two dimensional earth ($\sigma(z,y)$ say) the impedance becomes a 2x2 tensor relating the horizontal electric and magnetic fields (see section 2.2). This is because certain 2-D and 3-D models may cause currents to flow parallel as well as perpendicular to a primary inducing magnetic field. The tensor formulation is advantageous since in the principal axes frame of a 2-D structure the impedances along and across strike do not depend on the source field polarization. Section 2.4 describes rotation properties of the tensor which determine the principal axes of the 2-D structure and distinguish between 2-D and the very much more difficult 3-D models (Vozoff, 1972).

Unfortunately, for practical applications, constraints imposed upon $\sigma(z)$ by the MT method are not too restrictive. The resolving power of MT data and the uniqueness of

constructed models are two problems which have as yet no rigorous solutions. Qualitatively, it is known that high resolution is achieved for conductive zones where the fields are rapidly attenuated. Resistive layers are more poorly defined. Furthermore, below a certain depth even a long period datum is insensitive to high conductivity since the fields have decayed to very small amplitudes (Parker, 1982). The second problem of model uniqueness occurs because we can only secure a finite number of inaccurate MT responses. Using these data, any inversion algorithm can return only a few of the infinitely many conductivity profiles which fit the data equally well. Within a particular routine there may be parameters to vary which result in slightly different models. However, a different inversion scheme is likely to return models which are globally distinct and which cannot be found by the other algorithm (see Chapter 4). Thus, non-uniqueness prohibits over-interpretation of minute structures visible on a single $\sigma(z)$ profile (Parker et al, 1983). Inferring what structures are common to all models which fit the data is difficult for non-linear inverse problems such as MT. Rather than dealing with a profusion of $\sigma(z)$ curves there may be more profit in quantifying the bounds on the average conductivity between two depths or the range of conductance models allowed by the data (Oldenburg, 1983). The conductance is simply the integral of the conductivity from the surface down to a certain depth. The global bounds on the conductance presented in section 4.4 give a measure of the resolution of the data as a function of depth.

Electrical conductivity is an important property since it is related to other geophysical quantities such as temperature, partial melting and petrology. These, in turn, provide constraints on structural and dynamic models of the earth's crust and mantle. Results from ocean bottom instruments placed above 1, 30 and 72 my old lithosphere by Law and Greenhouse (1981) and Filloux (1967,1977) vary with age in a way that is consistent with the theories of sea-floor spreading. Data from these three sites were inverted and compared by Oldenburg (1981) to reveal a correlation between conductivity and lithospheric age also noted by Filloux (1980). The pattern reported by Oldenburg (1981) was that for increasing age the depth to a conductive region increased from 70 to 120 to 180 km, for these data sets. The conductivity highs are well correlated with the seismic low velocity zone and may be representative of a partially molten asthenosphere. Results from the new study above 3 my old lithosphere disrupt this coherent picture somewhat by persistently showing a fairly uniform high conductivity zone from the surface down to about 100 km depth. Subsequent analysis of the previous three data sets using different inversion schemes has shown the observed trends are not as strong as initially believed. But even allowing for the high degree of non-uniqueness inherent in the MT method it appears that the 3 my datum is strikingly discordant (see section 5.1).

1.2 The Experiment

Several ocean bottom magnetometers (OBM's) were deployed

off Vancouver Island by L.K.Law during the summer of 1980. Law and Greenhouse (1981) describe the instrument design. The one used for this study was furthest from the coast in about 2760m of water and above 3 my old lithosphere (see Figure 1). It recorded three orthogonal components of the magnetic field from 23 July to 26 August 1980. The sensors were flux gate magnetometers accurate to 1 nT. Every minute the component values were recorded on digital tape. Tilt meters within the instrument package showed the OBM's horizontal axes to be about one degree from level so no correction was made to the recorded field values. However, a correction for the orientation of the horizontal axes was made to align them with geomagnetic north (H) and east (D). The relative amplitude of the horizontal components during magnetically quiet times determined this rotation angle as 20.6° clockwise.

An example of 4 days of rotated OBM data is shown in Figure 2. The two horizontal channels (H and D) are plotted below the vertical channel (Z). The time on the horizontal axis is in hours since 0701 23 July 1980 UT. The record is dominated by the diurnal Sq variation with peak to peak amplitudes of up to 100 nT on the D component. Superimposed on these regular oscillations is a sudden commencement magnetic storm beginning near hour 52.

Records from the Victoria Geomagnetic Observatory (VIC) are required to calculate the sea-floor impedance (see section 2.5). There were two gaps in the VIC data which totalled 9 hours. These missing hours are filled by a signal most similar to all 33 daily records. That common signal was found using

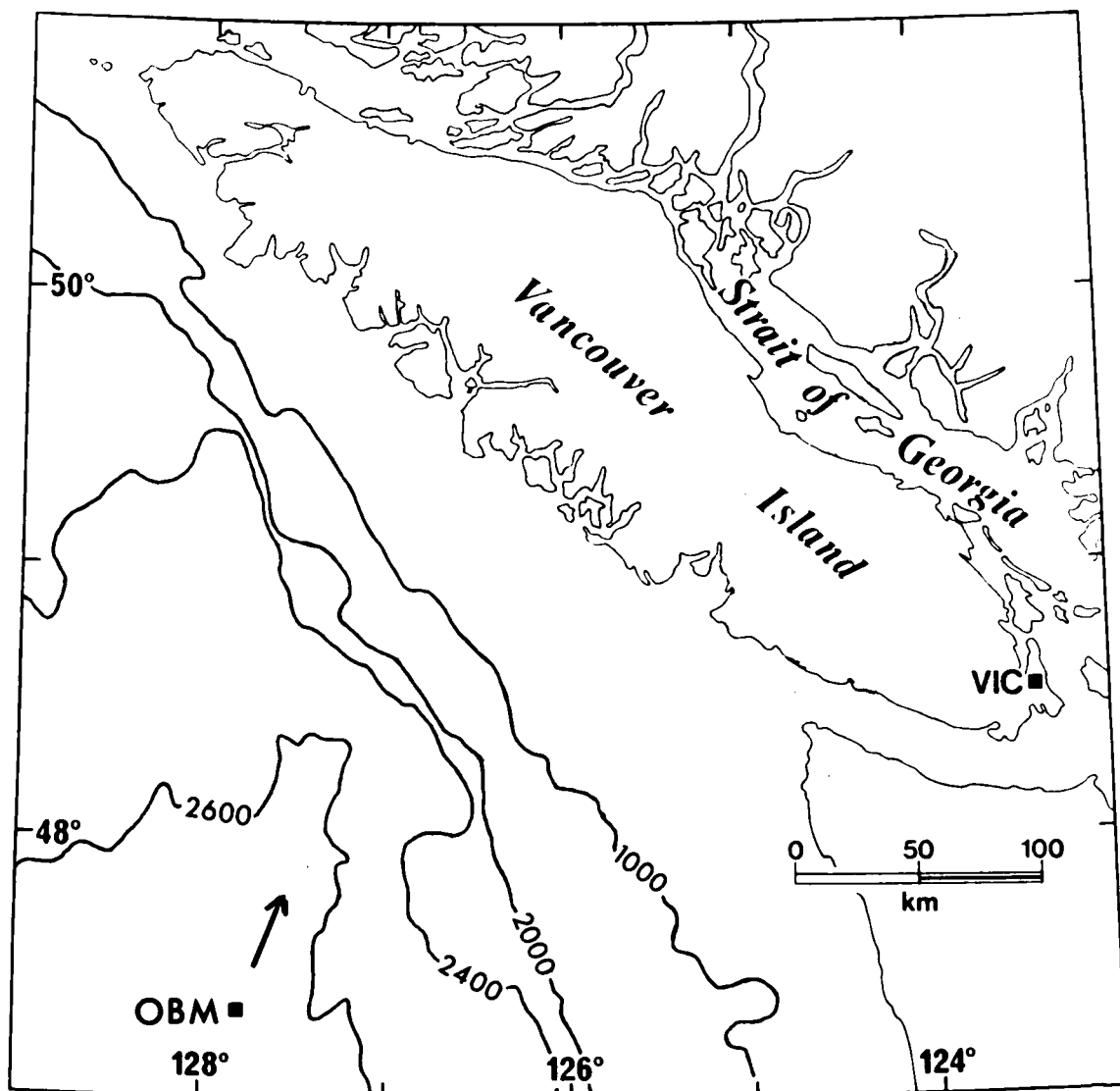


Figure 1.
Location map for the ocean bottom magnetometer (OBM) and the Victoria Geomagnetic Observatory (VIC). Bathymetric contours are in meters. The arrow near the OBM points towards the north magnetic pole.

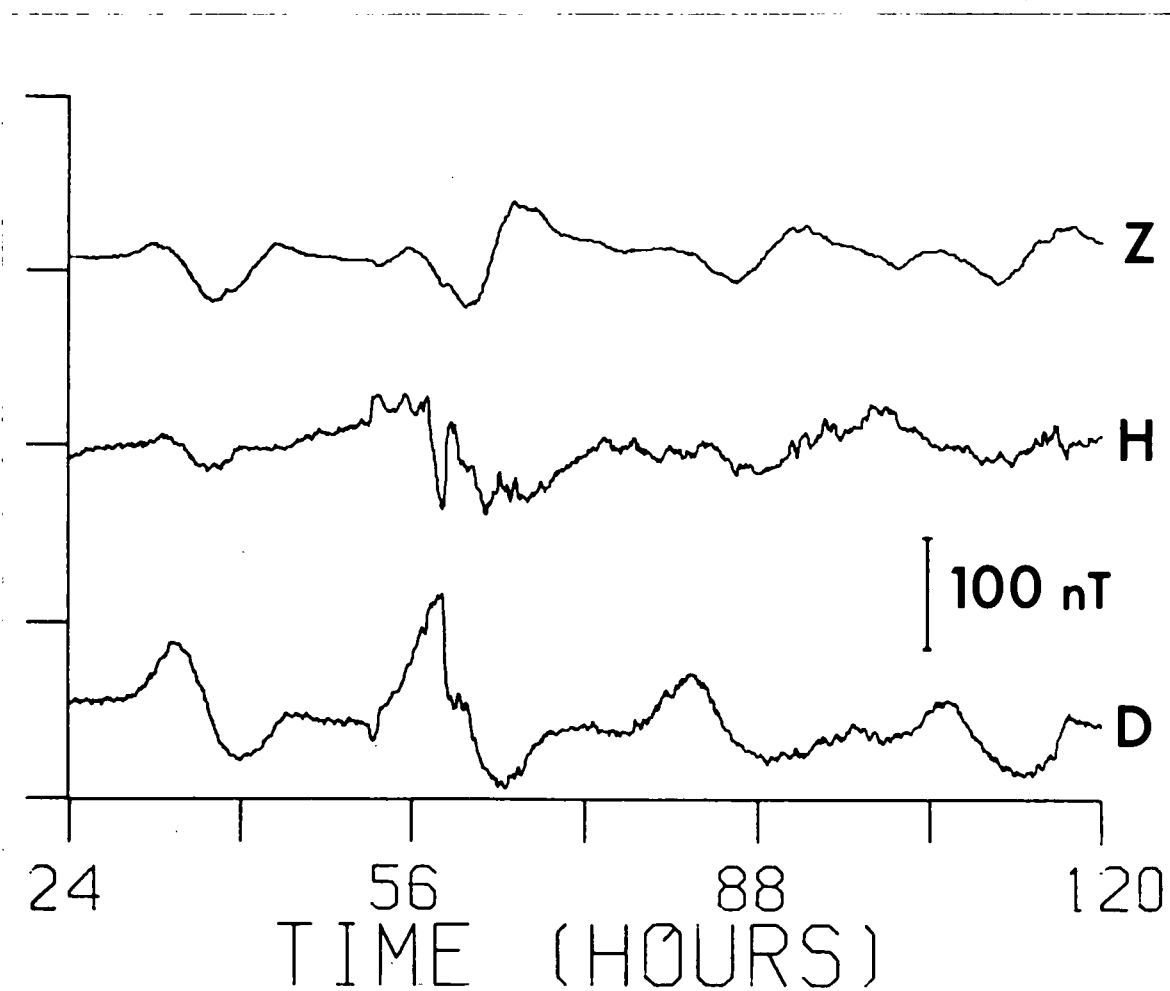


Figure 2.

Four days of the three component OBM data. D is geomagnetic east, H is geomagnetic north and Z is vertically down.

the method described by Oldenburg, Scheuer and Levy (1982). Each daily trace is decomposed into a linear combination of the same orthonormal basis functions. The common signal is then that linear combination of basis functions which minimizes the error between it and all the recorded data. The magnitude of a coefficient in the linear combination indicates the relative importance of the associated basis function. Small coefficients have basis functions which are weakly correlated with the daily traces and may contain significant amounts of noise. Large coefficients multiply basis functions which dominate every trace and have large signal to noise ratios. For this application, one coefficient in the linear combination is much larger than all the others combined. The common signal is constructed from the principal component basis function corresponding to this largest coefficient. Note that if all basis functions are used then the method reduces to a simple average of the daily records. The appropriate parts of the principal component were inserted into the two data gaps with a minimum of offset at the endpoints. Traces recorded at VIC corresponding to those of Figure 2 are shown in Figure 3. The reduced high frequency content at OBM relative to VIC is caused by the strongly conducting, highly attenuating ocean layer (see Figure 7).

An example of one channel of the entire 33 day OBM data set is given in Figure 4. Each subgraph is one day long, is individually normalized, and begins at a time near local midnight. Magnetic storms disturb the record over days 2 to 5 and 24 to 27.

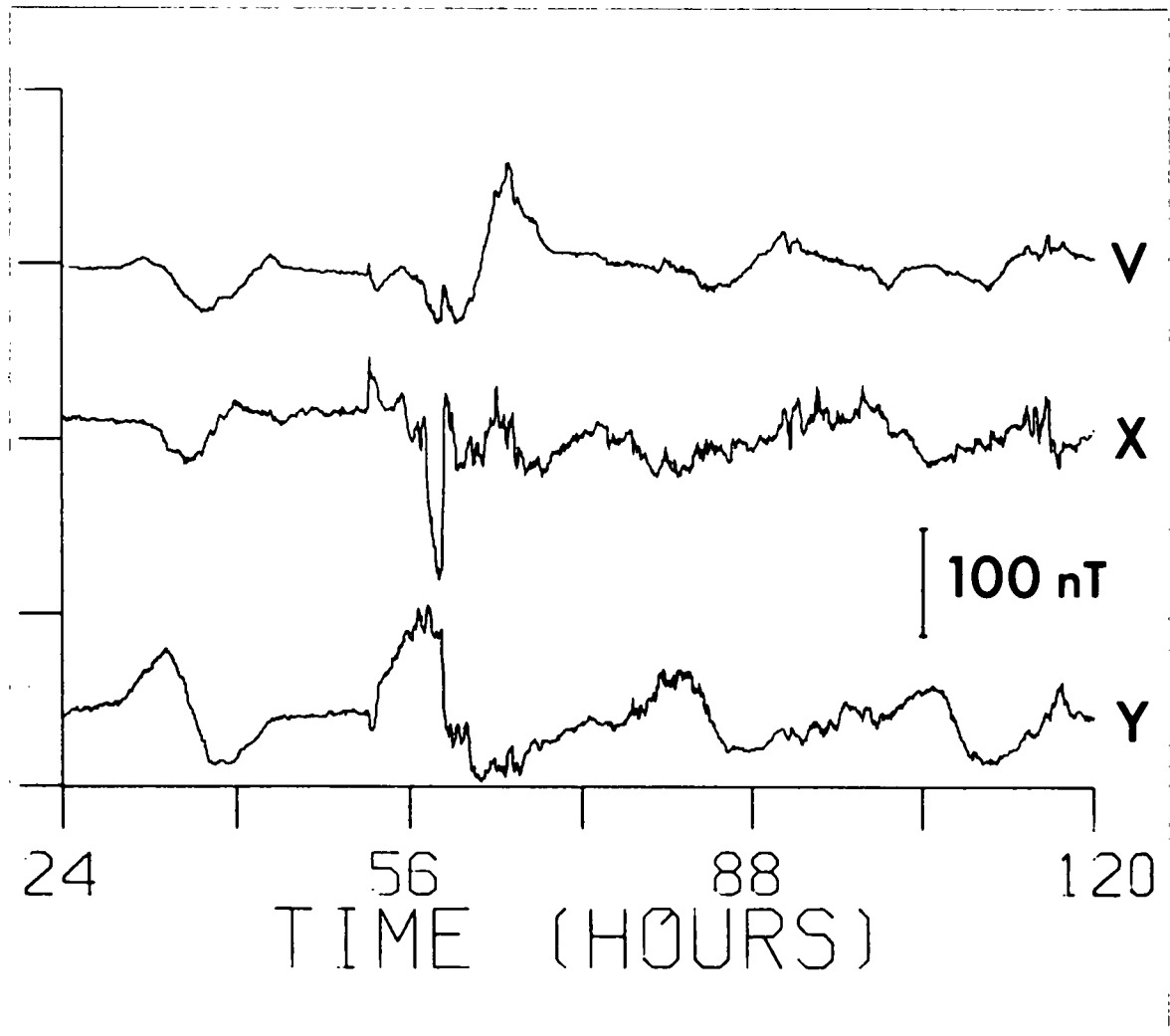
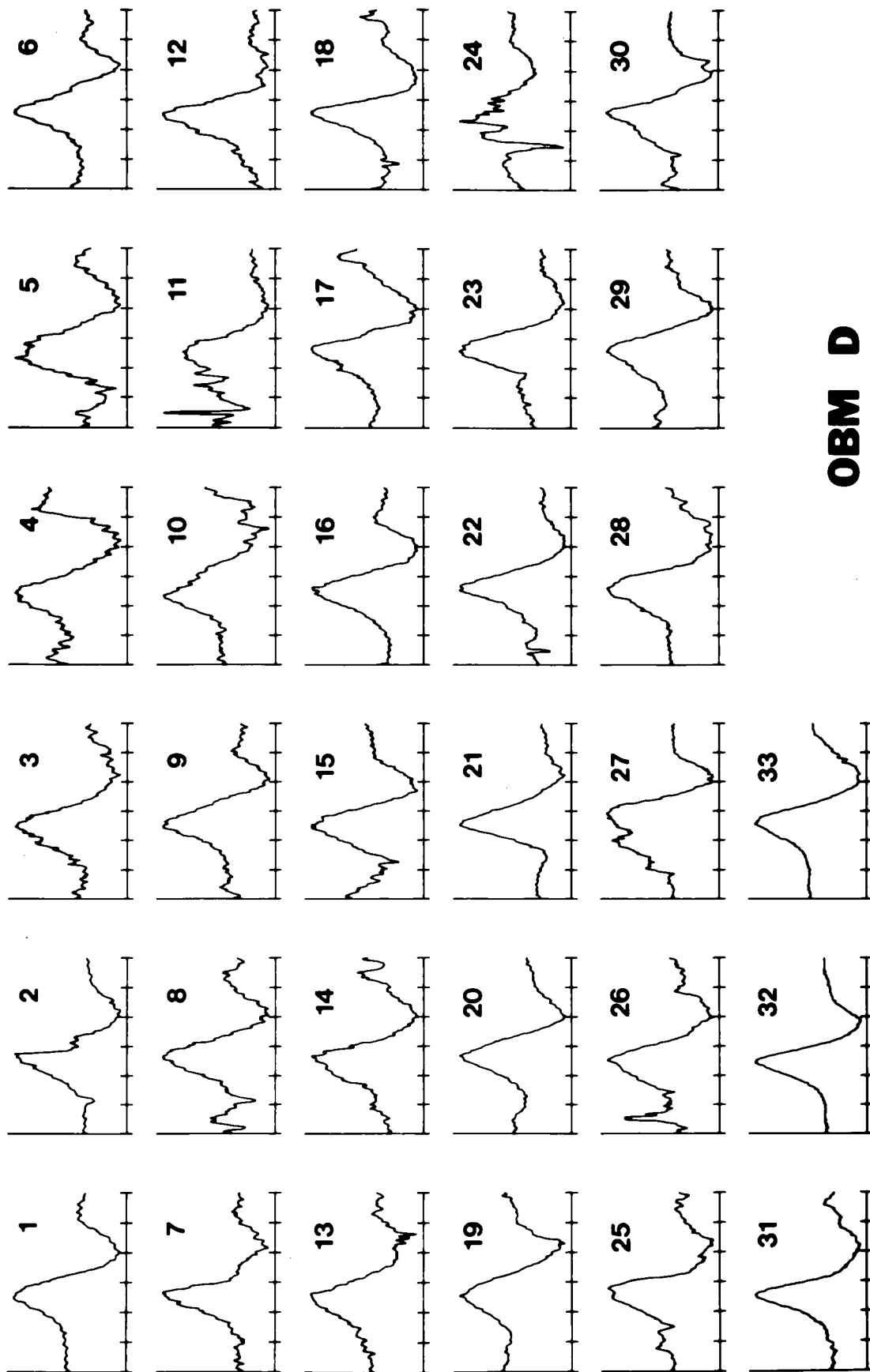


Figure 3.

Four days of data from VIC. Y is geomagnetic east, X is geomagnetic north and V is vertically down.

Figure 4.

The complete 33 day record of the OBM horizontal D channel. Each day is individually normalized and begins about 1.5 hours before local midnight.

**OBM D**

CHAPTER 2 THEORY OF THE MAGNETOTELLURIC METHOD

This chapter contains theory relevant to the MT method in general and to this ocean bottom application in particular. Maxwell's equations are used to derive the MT equations which govern the diffusion of harmonic electromagnetic waves into the conducting earth. In section 2.1 and 2.3 the impedance at the surface of a simple layered earth is derived. Its value is obtained from a recursion formula in terms of the impedances or reflection coefficients at lower levels. In a two dimensional earth a 2×2 impedance tensor relates the horizontal electric and magnetic fields (section 2.2). The tensor formulation is more stable since the principal impedances derived from it do not depend on the sensor orientation or on the total field polarization. The rotational properties of the tensor outlined in section 2.4 give the principal directions of a 2-D earth and distinguish between this and a more complex 3-D earth structure. The filtering effect of the highly conducting ocean on the diffusing fields is considered and exploited to calculate sea-floor impedances from magnetic fields alone (section 2.5). Lastly, in sections 2.6 and 2.7, the plane wave and flat earth approximations are examined and found to be valid for the period range used in this study.

2.1 MT Fields in a One Dimensional Earth

When the earth model is restricted to be composed of a stack of uniform, horizontal, flat layers then it is termed one dimensional since the conductivity varies only with depth.

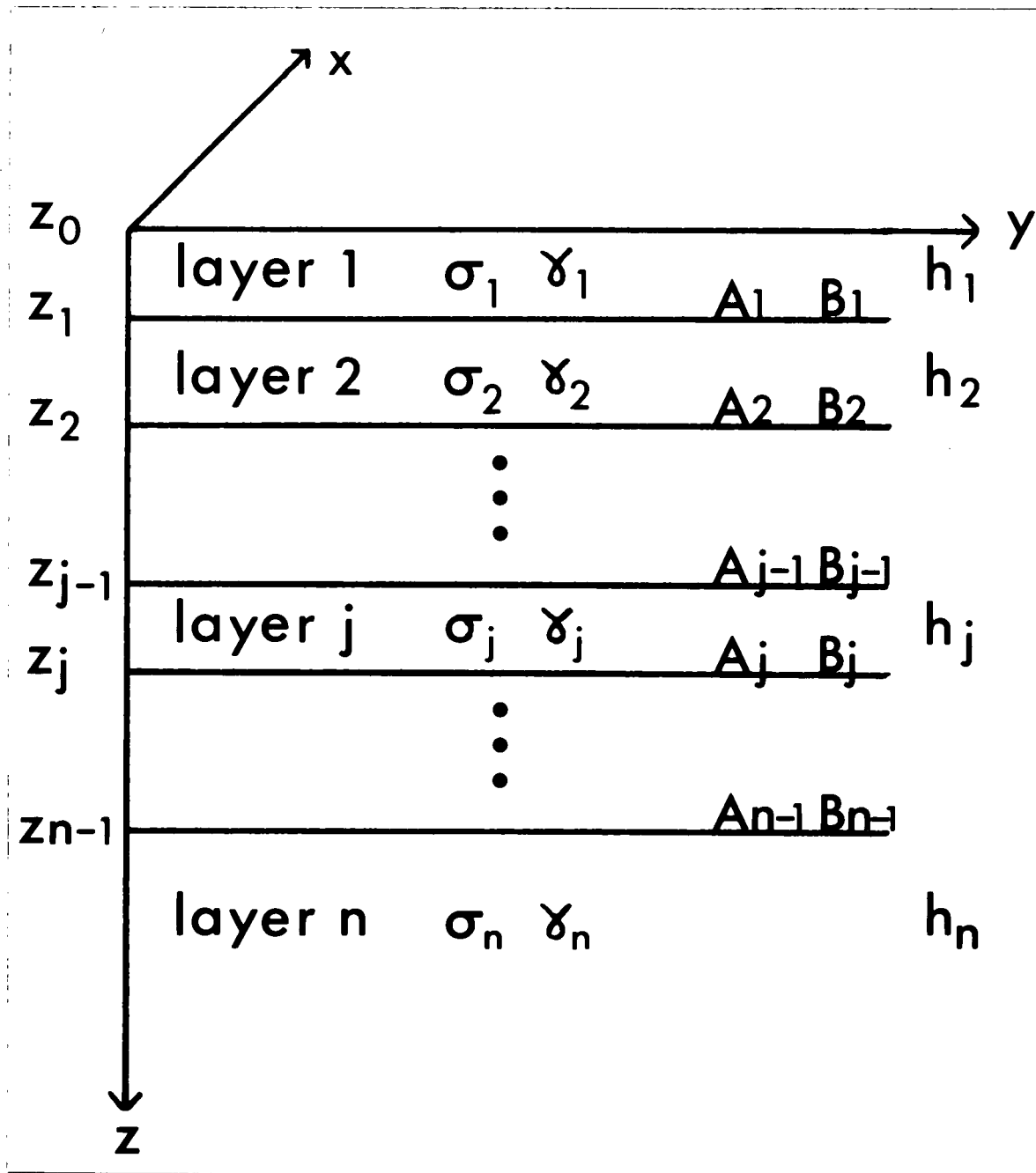


Figure 5.

The one dimensional model with notation used in this thesis. Within layer j of thickness h_j the conductivity is σ_j , the parameter $\gamma_j = \sqrt{i\mu\omega\sigma_j}$ and A_j and B_j are the amplitudes of the downgoing and upgoing waves, respectively, at the level z_j . Layer n is a halfspace of infinite thickness. B_{n-1} is equal to zero.

An example of such an earth is illustrated in Figure 5. If the incident EM fields are plane waves and they are refracted to the vertical then simple diffusion equations pilot their voyage into the earth. Furthermore, the impedance $Z(\omega)$ measured at the surface is compactly expressed as a recurrence relation in terms of the layer parameters.

We begin with the ubiquitous Maxwell equations

$$\text{curl } \underline{E} = -\mu \partial \underline{H} / \partial t$$

$$\text{curl } \underline{H} = \sigma(z) \underline{E} + \epsilon \partial \underline{E} / \partial t$$

$$\text{div } \underline{E} = 0$$

$$\text{div } \underline{H} = 0 \quad (2.1)$$

where \underline{E} is the electric field vector, \underline{H} is the magnetic field vector, μ is the magnetic permeability (assumed constant for all layers and equal to the free space value $\mu_0 = 4\pi \times 10^{-7}$ H/m), ϵ is the dielectric constant (equal to 8.86×10^{-12} F/m), and $\sigma(z)$ is the conductivity. Assuming the fields are quasi-periodic, that is, $\underline{E} \sim \exp(+i\omega t)$ and $\underline{H} \sim \exp(+i\omega t)$, and all transients have decayed away, we can write the first two equations in (2.1) as

$$\text{curl } \underline{E} = -i\mu\omega \underline{H}$$

$$\text{curl } \underline{H} = \sigma(z) \underline{E} + i\epsilon\omega \underline{E} \quad (2.2)$$

Because the product $\epsilon\omega$ is very small compared to $\sigma(z)$ (Keller and Frischknecht 1966, p212) the second term in the last equation may be dropped. Moreover, the fields in a 1-D earth do not change with coordinates x or y because of the vertically diffusing plane wave assumption. Therefore, derivatives with respect to x and y vanish and equations (2.2) become

$$\begin{aligned}
dE_y/dz &= +i\mu\omega H_x & dH_y/dz &= -\sigma E_x \\
dE_x/dz &= -i\mu\omega H_y & dH_x/dz &= +\sigma E_y \\
0 &= H_z & 0 &= E_z
\end{aligned} \tag{2.3}$$

Differential equations for each horizontal component of \underline{E} and \underline{H} are found from equations (2.3) to be

$$\begin{aligned}
d^2 E_x/dz^2 &= \gamma^2 E_x & d^2 H_x/dz^2 &= \gamma^2 H_x \\
d^2 E_y/dz^2 &= \gamma^2 E_y & d^2 H_y/dz^2 &= \gamma^2 H_y
\end{aligned} \tag{2.4}$$

where $\gamma^2 = i\mu\omega\sigma(z)$. Solutions to these diffusion equations all have the same form within layers where γ^2 is constant.

For a halfspace of constant conductivity σ_0 , a typical solution is

$$E_x(z) = A e^{-\gamma z + i\omega t} + B e^{+\gamma z + i\omega t}$$

where $\gamma = (1+i)(\mu\omega\sigma_0/2)^{1/2} = (1+i)\beta$ and A and B are constants. The solution is a linear combination of two independent decaying waves, one travelling down (the first term) and the other travelling up (the second term). For a halfspace there is no upgoing wave since there are no sources within the earth and there are no horizons to reflect the downgoing wave back towards the surface. Therefore, in the linear combination above, the coefficient B=0. The remaining term is

$$A e^{-\beta z} e^{i(\omega t - \beta z)} = E_x(0) e^{-\beta z} e^{-i\beta z}$$

which represents a wave decaying as it travels down into the halfspace. The rate of attenuation is governed by the parameter β . At a depth $z=1/\beta$ the wave has decayed to $1/e$ of its surface amplitude $E_x(0)$. Traditionally, $\delta=1/\beta$ is called the skin depth. For a given halfspace conductivity σ_0 , δ is small for high frequencies and large for low frequencies.

Hence, progressively longer periods sample progressively deeper structures. Alternatively, for a fixed frequency ω , δ is smaller for larger conductivities. This implies rapid field attenuation within conducting layers. For a fixed time t , the phase of the electric field changes by 2π radians from its surface value when $\beta z = 2\pi$ or $z = 2\pi\delta$. This distance is a measure of the wavelength of the diffusing field.

Within layer j of a more complex, layered 1-D earth we write for $z_j \geq z \geq z_{j-1}$

$$E_{xj}(z) = A_j e^{+i\omega t + \gamma_j(z_j - z)} + B_j e^{+i\omega t - \gamma_j(z_j - z)} \quad (2.5)$$

where $\gamma_j = (1+i)(\mu\omega\sigma_j/2)^{1/2} = (1+i)\beta_j$, and A_j and B_j are the amplitudes of the downgoing and upgoing waves respectively as they cross the level z_j . The corresponding solution for $H_{yj}(z)$ is found from equations (2.3) and (2.5) as

$$H_{yj}(z) = -\frac{\gamma_j}{i\mu\omega} [A_j e^{+i\omega t + \gamma_j(z_j - z)} - B_j e^{+i\omega t - \gamma_j(z_j - z)}] \quad (2.6)$$

again for $z_j \geq z \geq z_{j-1}$. The quantity of interest is the impedance $Z_{xy}(z)$ which is the ratio of the electric to the magnetic field and as such it is independent of changes in the incident field strength.

$$Z_{xy}(z) = \frac{E_{xj}(z)}{H_{yj}(z)} = \frac{i\mu\omega}{\gamma_j} \frac{A_j e^{\gamma_j(z_j - z)} + B_j e^{-\gamma_j(z_j - z)}}{A_j e^{\gamma_j(z_j - z)} - B_j e^{-\gamma_j(z_j - z)}} \quad (2.7)$$

To find the impedance at the surface of a 1-D earth, $Z_{xy}(0)$, A_j and B_j must be calculated. Values for these constants are found by considering Z_{xy} at two levels within the same $\gamma^2 = \text{constant}$ layer. The identity $(A_j/B_j)^{1/2} = \exp(\ln(A_j/B_j)^{1/2})$ is useful in producing

$$Z_{xy}(z) = \frac{i\mu\omega}{r_j} \coth[(\ln(A_j/B_j))^{\frac{1}{2}} + r_j(z_j - z)]$$

within layer j . At the bottom of this layer $z=z_j$ and

$$Z_{xy}(z_j) = \frac{i\mu\omega}{r_j} \coth[(\ln(A_j/B_j))^{\frac{1}{2}}]$$

At the top of the j 'th layer $z=z_{j-1}$ and

$$Z_{xy}(z_{j-1}) = \frac{i\mu\omega}{r_j} \coth[(\ln(A_j/B_j))^{\frac{1}{2}} + r_j h_j]$$

where $h_j = z_j - z_{j-1}$ is the thickness of the j 'th layer. Combining these last two equations gives

$$Z_{xy}(z_{j-1}) = \frac{i\mu\omega}{r_j} \coth\left[\coth^{-1}\left(\frac{r_j Z_{xy}(z_j)}{i\mu\omega}\right) + r_j h_j\right] \quad (2.8)$$

This shows that the impedance at the top of a layer may be written in terms of the impedance at the bottom of that layer. Furthermore, since the horizontal components of \underline{E} and \underline{H} are continuous across layer boundaries, Z_{xy} is continuous. So $Z_{xy}(0)$ is found by stepping up recursively through the model layers beginning with the boundary condition at the top of the basal halfspace

$$Z_{xy}(z_{n-1}) = i\mu\omega/r_n \quad (2.9)$$

since in equation (2.8) $h_n = \infty$ and $\coth(\infty) = 1$. For a layer over a halfspace let $z_{j-1} = z_0 = 0$ and $z_j = z_1 = h_1$ in equation (2.8). Then

$$Z_{xy}(0) = \frac{i\mu\omega}{r_1} \coth\left[r_1 h_1 + \coth^{-1}\left(\frac{Z_1 r_1}{i\mu\omega}\right)\right] \quad (2.10)$$

where $Z_1 = Z_{xy}(z_1) = i\mu\omega/r_2$. Keller and Frischknecht (1966) and Kaufman and Keller (1981), for example, present the simple extension of this formula for any number of layers over a halfspace.

Another useful equation for $Z_{xy}(0)$ is obtained by recasting equation (2.8) in terms of a continued fraction of reflection coefficients. This representation is central to the three inversion programmes of Parker and Whaler (1981) and that of Fischer et al (1981). Since the impedance is continuous across a layer interface we use equation (2.7) to write

$$\begin{aligned} Z_{j-1}(z_{j-1}) &= Z_j(z_{j-1}) = \frac{i\mu\omega A_{j-1} + B_{j-1}}{\gamma_{j-1} A_{j-1} - B_{j-1}} \\ &= \frac{i\mu\omega A_j e^{+\gamma_j h_j} + B_j e^{-\gamma_j h_j}}{\gamma_j A_j e^{+\gamma_j h_j} - B_j e^{-\gamma_j h_j}} \end{aligned}$$

where $h_j = z_j - z_{j-1}$. This is rewritten as

$$\begin{aligned} A_{j-1} [R_{(j-1)j} A_j e^{+\gamma_j h_j} + B_j e^{-\gamma_j h_j}] \\ = B_{j-1} [A_j e^{+\gamma_j h_j} + R_{(j-1)j} B_j e^{-\gamma_j h_j}] \end{aligned}$$

where the reflection coefficient

$$R_{(j-1)j} = \frac{\gamma_{j-1} - \gamma_j}{\gamma_{j-1} + \gamma_j} = \frac{\sqrt{\sigma_{j-1}} - \sqrt{\sigma_j}}{\sqrt{\sigma_{j-1}} + \sqrt{\sigma_j}} \quad (2.11)$$

The ratio of upgoing to downgoing amplitudes is

$$\frac{B_{j-1}}{A_{j-1}} = \frac{R_{(j-1)j} A_j e^{+\gamma_j h_j} + B_j e^{-\gamma_j h_j}}{A_j e^{+\gamma_j h_j} + R_{(j-1)j} B_j e^{-\gamma_j h_j}}$$

Multiplying top and bottom by $R_{(j-1)j}$ and adding (1-1) to the numerator gives, after another few steps,

$$\frac{B_{j-1}}{A_{j-1}} = 1/R_{(j-1)j} + \frac{(1 - 1/R_{(j-1)j}^2) e^{+2\gamma_j h_j}}{e^{+2\gamma_j h_j}/R_{(j-1)j} + B_j/A_j} \quad (2.12)$$

which is the desired continued fraction at last. From equation (2.7), within layer j

$$Z_{xy}(z) = \frac{i\mu\omega \left(1 + \frac{B_j}{A_j} e^{-2\gamma_j \Delta z}\right)}{\gamma_j \left(1 - \frac{B_j}{A_j} e^{-2\gamma_j \Delta z}\right)}$$

where $\Delta z = z_j - z$. The boundary condition is that $B_{n-1} = 0$ since there is no reflected wave from the bottomless basal halfspace. The final surface impedance is

$$Z_{xy}(0) = \frac{i\mu\omega \left(1 + \frac{B_1}{A_1} e^{-2\gamma_1 h_1}\right)}{\gamma_1 \left(1 - \frac{B_1}{A_1} e^{-2\gamma_1 h_1}\right)} \quad (2.13)$$

For a uniform halfspace $B_1 = 0$, $h_1 = \infty$ and $Z_{xy}(0) = i\mu\omega/\gamma_1$, which agrees with equation (2.9). For a layer over a halfspace $B_2 = 0$ and from equation (2.12)

$$\frac{B_1}{A_1} = \frac{1}{R_{12}} + \frac{1 - 1/R_{12}^2}{1/R_{12}} = R_{12} = \frac{\gamma_1 - \gamma_2}{\gamma_1 + \gamma_2}$$

Hence

$$Z_{xy}(0) = \frac{i\mu\omega \left(1 + R_{12} e^{-2\gamma_1 h_1}\right)}{\gamma_1 \left(1 - R_{12} e^{-2\gamma_1 h_1}\right)} \quad (2.14)$$

The foregoing discussion from equation (2.5) onwards calculated Z_{xy} from E_x and H_y . There is an equivalent development for Z_{yx} derived from E_y and H_x . In fact $Z_{yx} = -Z_{xy}$ for the 1-D model assumed here.

2.2 MT Fields in a Two Dimensional Earth

A hypothetical 2-D model is presented in Figure 6. In the strike direction x there is no structural variation. Hence,

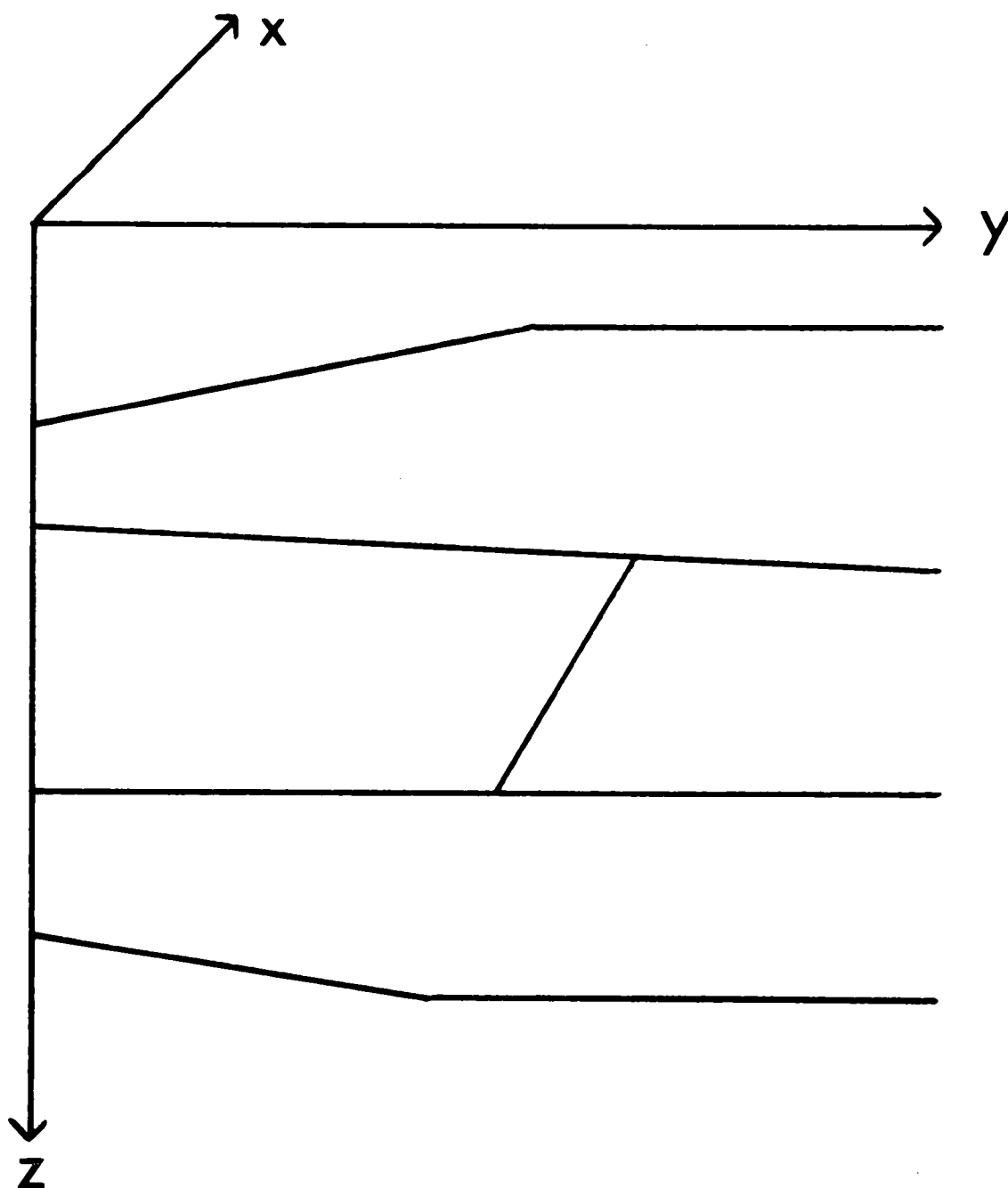


Figure 6.
A two dimensional earth with strike direction x .

for vertically diffusing plane waves derivatives with respect to x vanish. The Maxwell equations (2.2) become

$$\begin{aligned}
 \frac{\partial E_z}{\partial y} - \frac{\partial E_y}{\partial z} &= -i\mu\omega H_x \\
 \frac{\partial E_x}{\partial z} &= -i\mu\omega H_y \\
 -\frac{\partial E_x}{\partial y} &= -i\mu\omega H_z \\
 \frac{\partial H_z}{\partial y} - \frac{\partial H_y}{\partial z} &= \sigma E_x \\
 \frac{\partial H_x}{\partial z} &= \sigma E_y \\
 -\frac{\partial H_x}{\partial y} &= \sigma E_z
 \end{aligned} \tag{2.15}$$

Usually the incident primary field will be elliptically polarized in the x - y plane and will induce complex secondary fields because of the lateral inhomogeneities. A linear impedance tensor, $\underline{\underline{Z}}$, relating the total electric and magnetic fields admits all possible influences between components. The linearity results from the linear Maxwell equations. Thus, we assume

$$\underline{\underline{E}} = \underline{\underline{Z}} \underline{\underline{H}} \text{ or } \begin{pmatrix} E_x \\ E_y \\ E_z \end{pmatrix} = \begin{pmatrix} Z_{11} & Z_{12} & Z_{13} \\ Z_{21} & Z_{22} & Z_{23} \\ Z_{31} & Z_{32} & Z_{33} \end{pmatrix} \begin{pmatrix} H_x \\ H_y \\ H_z \end{pmatrix}$$

Similarly, we postulate an admittance tensor $\underline{\underline{Y}}$ where $\underline{\underline{H}} = \underline{\underline{Y}} \underline{\underline{E}}$. Simplifications result from decomposing the primary field into two independent polarized fields. The first, E-polarization, has the electric field vector along the strike direction. Thus, $\underline{\underline{E}} = (E_x, 0, 0)$ and $\underline{\underline{H}} = (0, H_y, H_z)$. The second, H-polarization, has the magnetic field vector parallel to strike with $\underline{\underline{E}} = (0, E_y, E_z)$ and $\underline{\underline{H}} = (H_x, 0, 0)$. These two polarizations are important because a primary field in either state induces a secondary field in that same state via equations (2.15). Therefore, the total field, primary plus secondary, decomposes into E- and H-polarizations. The corresponding impedance relationships are

$$\text{E-pol} \quad \begin{pmatrix} E_x \\ 0 \\ 0 \end{pmatrix} = \begin{pmatrix} \dots & Z_{22} & Z_{23} \\ \dots & Z_{55} & Z_{56} \\ \dots & Z_{88} & Z_{89} \end{pmatrix} \begin{pmatrix} 0 \\ H_y \\ H_z \end{pmatrix}$$

$$\text{H-pol} \quad \begin{pmatrix} 0 \\ E_y \\ E_z \end{pmatrix} = \begin{pmatrix} 0 & \dots & \dots \\ Z_{44} & \dots & \dots \\ Z_{77} & \dots & \dots \end{pmatrix} \begin{pmatrix} H_x \\ 0 \\ 0 \end{pmatrix}$$

where \dots indicates an unconstrained element. The 3×3 \underline{Z} tensor collapses to a 2×2 form because of the following arguments. According to the admittance tensor, H_z is a linear combination of E_x , E_y , and E_z . But from \underline{Z} these field components are, in turn, a linear combination of H_x , H_y , and H_z . So we write

$$H_z = A H_x + B H_y$$

where A and B are complex constants. For E-polarization $H_x=0$ and so $H_z=BH_y$. With H_z proportional to H_y the third column of \underline{Z} is incorporated into the second column. The resulting 3×2 matrix now has its second and third rows linearly dependent so one row is discarded. Hence,

$$\text{E-pol} \quad \begin{pmatrix} E_x \\ 0 \end{pmatrix} = \begin{pmatrix} \dots & Z_{xy} \\ \dots & 0 \end{pmatrix} \begin{pmatrix} 0 \\ H_y \end{pmatrix}$$

A similar argument for H-polarization yields

$$\text{H-pol} \quad \begin{pmatrix} 0 \\ E_y \end{pmatrix} = \begin{pmatrix} 0 & \dots \\ Z_{yx} & \dots \end{pmatrix} \begin{pmatrix} H_x \\ 0 \end{pmatrix}$$

To completely specify all four elements of the 2×2 impedance tensor the total field must be composed of EM waves of both polarizations. In general then,

$$\begin{pmatrix} E_x \\ E_y \end{pmatrix} = \begin{pmatrix} 0 & Z_{xy} \\ Z_{yx} & 0 \end{pmatrix} \begin{pmatrix} H_x \\ H_y \end{pmatrix} \quad (2.16)$$

In reference frames which do not have axes parallel and perpendicular to strike the diagonal elements are non-zero (see section 2.4 for rotation properties of the impedance

tensor).

2.3 Derivation of the Impedance Tensor for 1-D Models

The heuristic arguments for a 2×2 \underline{Z} given in the preceeding section are supported by a more rigorous development following Loewenthal and Landisman (1973). These authors derived from first principles the impedance tensor for an anisotropic layered medium. In this section it is shown (for 1-D isotropic models) that if a 2×2 \underline{Z} is assumed then using just the electric and magnetic fields reasonable expressions for each element are possible.

Equations (2.5) and (2.6) along with similar expressions for E_y and H_x are put in matrix form and the $\exp(+i\omega t)$ factor is dropped. Thus,

$$\begin{pmatrix} E_{x_j}(z) \\ E_{y_j}(z) \end{pmatrix} = \begin{pmatrix} e^{+\gamma_j \Delta z} & 0 \\ 0 & e^{+\gamma_j \Delta z} \end{pmatrix} \begin{pmatrix} E_j^+ x \\ E_j^+ y \end{pmatrix} + \begin{pmatrix} e^{-\gamma_j \Delta z} & 0 \\ 0 & e^{-\gamma_j \Delta z} \end{pmatrix} \begin{pmatrix} E_j^- x \\ E_j^- y \end{pmatrix} \quad (2.17)$$

$$\frac{i\mu\omega}{\gamma_j} \begin{pmatrix} H_{x_j}(z) \\ H_{y_j}(z) \end{pmatrix} = \begin{pmatrix} 0 & -e^{+\gamma_j \Delta z} \\ e^{+\gamma_j \Delta z} & 0 \end{pmatrix} \begin{pmatrix} E_j^+ x \\ E_j^+ y \end{pmatrix} - \begin{pmatrix} 0 & -e^{-\gamma_j \Delta z} \\ e^{-\gamma_j \Delta z} & 0 \end{pmatrix} \begin{pmatrix} E_j^- x \\ E_j^- y \end{pmatrix} \quad (2.18)$$

where $\Delta z = z_j - z$, $z_j \geq z \geq z_{j-1}$ and A_j and B_j have been replaced by E_j^+ and E_j^- which are the downgoing and upgoing electric field amplitudes, respectively, at the level z_j . Note that if \underline{E} and \underline{H} are both written as a 2×2 tensor times a common vector \underline{C} then a 2×2 impedance tensor \underline{Z} is found from the following. Let

$$\underline{E} = \underline{W}_1 \underline{C} \quad \text{and} \quad \underline{H} = (\gamma/i\mu\omega) \underline{W}_2 \underline{C}$$

where \underline{W}_1 and \underline{W}_2 are 2×2 tensors as yet unknown. Rewrite the second expression as $\underline{C} = (i\mu\omega/\gamma) \underline{W}_2^{-1} \underline{H}$ and substitute into

the first expression

$$\underline{E} = (i\mu\omega/\gamma) \underline{W}_1 \underline{W}_2^{-1} \underline{H}$$

Therefore,

$$\underline{Z} = \frac{i\mu\omega}{\gamma} \underline{W}_1 \underline{W}_2^{-1} \quad (2.19)$$

So the impedance tensor is simply a combination of the tensors which premultiply the common vector, \underline{C} . In search of this common vector we first recall that the impedance is continuous across an interface so we write

$$\underline{E}_j(z_j) = \underline{Z}_{j-1}(z_j) \underline{H}_j(z_j)$$

Substitute equations (2.17) and (2.18) into this last expression and note that $\Delta z=0$

$$\begin{aligned} \underline{E}_j(z_j) &= \underline{I} \underline{E}_j^+ + \underline{I} \underline{E}_j^- \\ &= \underline{Z}_{j-1}(z_j) \frac{\gamma_j}{i\mu\omega} \underline{G} (\underline{E}_j^+ - \underline{E}_j^-) \end{aligned}$$

where \underline{I} is the 2x2 identity matrix and

$$\underline{G} = \begin{pmatrix} 0 & -1 \\ 1 & 0 \end{pmatrix}$$

If we express \underline{E}_j^- in terms of \underline{E}_j^+ then the problem is solved with $\underline{C} = \underline{E}_j^+$. In fact, from the equation for $\underline{E}_j(z_j)$ above

$$\underline{E}_j^- = (\underline{I} - 2\underline{A}^{-1}) \underline{E}_j^+ \quad (2.20)$$

where

$$\underline{A} = \underline{Z}_{j-1}(z_j) \underline{G} \frac{\gamma_j}{i\mu\omega} + \underline{I}$$

Therefore,

$$\begin{aligned} \underline{E}_j(z_j) &= 2(\underline{I} - \underline{A}^{-1}) \underline{E}_j^+ \\ \underline{H}_j(z_j) &= \frac{2\gamma_j}{i\mu\omega} \underline{G} \underline{A}^{-1} \underline{E}_j^+ \end{aligned}$$

and from equation (2.19)

$$\underline{Z}_j(z_j) = \frac{i\mu\omega}{\gamma_j} (\underline{I} - \underline{A}^{-1}) [\underline{G} \underline{A}^{-1}]^{-1}$$

The impedance within the j'th layer is found by substituting \underline{E}_j^- from equation (2.20) into equations (2.17) and (2.18).

$$\underline{E}_j(z) = [e^{+\gamma_j \Delta z} \underline{I} + e^{-\gamma_j \Delta z} (\underline{I} - 2\underline{A}^{-1})] \underline{E}_j^+ = \underline{W}_1 \underline{E}_j^+$$

$$\underline{H}_j(z) = \frac{\gamma_j}{i\mu\omega} \underline{G} [e^{+\gamma_j \Delta z} \underline{I} - e^{-\gamma_j \Delta z} (\underline{I} - 2\underline{A}^{-1})] \underline{E}_j^+ = \frac{\gamma_j}{i\mu\omega} \underline{W}_2 \underline{E}_j^+$$

where $\Delta z = z_j - z$. Hence,

$$\underline{Z}_j(z) = \frac{i\mu\omega}{\gamma_j} \underline{W}_1 \underline{W}_2^{-1} \quad z_j \geq z \geq z_{j-1}$$

Example (1) A Halfspace

$$\underline{Z}_1(0) = \frac{i\mu\omega}{\gamma_1} \begin{pmatrix} 0 & 1 \\ -1 & 0 \end{pmatrix}$$

which agrees with the previous results of $Z_{xy} = -Z_{yx}$, $Z_{xx} = Z_{yy} = 0$ and equation (2.9).

Example (2) One Layer over a Halfspace

$$\underline{W}_1 = (e^{+\gamma_1 h_1} + R_{12} e^{-\gamma_1 h_1}) \underline{I}$$

$$\underline{W}_2 = (e^{+\gamma_1 h_1} - R_{12} e^{-\gamma_1 h_1}) \underline{G} \quad \text{and}$$

$$\underline{Z}_1(0) = \frac{i\mu\omega}{\gamma_1} \frac{1 + R_{12} e^{-2\gamma_1 h_1}}{1 - R_{12} e^{-2\gamma_1 h_1}} \begin{pmatrix} 0 & 1 \\ -1 & 0 \end{pmatrix}$$

This is a generalization of equation (2.14) with R_{12} defined as in equation (2.11).

2.4 Impedance Tensor Invariants and Symmetries

Once all the tensor elements are estimated (by techniques described in sections 3.2 and 3.3) it is important to select only those periods at which the tensor is consistent with certain theoretical constraints. When the constraints are violated it indicates the presence of large amounts of noise or a breakdown in one or more of the source and model assumptions. Other criteria for choosing periods compatible with the assumptions are presented in section 3.4.

Many of the tensor properties arise from an arbitrary rotation of the coordinate axes about the vertical. In a rotated frame the impedance tensor is

$$\underline{\underline{Z'}} = \underline{\underline{T}} \underline{\underline{Z}} \underline{\underline{T}}^T$$

where the superscript T indicates a transpose and

$$\underline{\underline{T}} = \begin{pmatrix} \cos\theta & \sin\theta \\ -\sin\theta & \cos\theta \end{pmatrix}$$

is the matrix which rotates the x-y axes of Figure 5 or 6 clockwise by $\theta > 0$. For any such similarity transformation

$$\text{tr}(\underline{\underline{Z}}) = \text{tr}(\underline{\underline{Z'}})$$

$$\det(\underline{\underline{Z}}) = \det(\underline{\underline{Z'}})$$

$$Z_{xy} - Z_{yx} = Z'_{xy} - Z'_{yx} \quad (2.21)$$

where the trace $\text{tr}(\underline{\underline{Z}}) = Z_{xx} + Z_{yy}$, and $\det(\underline{\underline{Z}})$ is the determinant of the matrix. We have already seen in sections 2.1 and 2.3 that for 1-D models $Z_{xx} = Z_{yy} = 0$ and $Z_{xy} = -Z_{yx}$. Section 2.2 showed that in the principal axes frame of 2-D models $Z_{xx} = Z_{yy} = 0$, and so for one or two dimensional models $\text{tr}(\underline{\underline{Z}}) = 0$ in any reference frame. During the course of a coordinate rotation through 180° the impedance tensor elements travel along ellipses in the

complex plane (Eggers, 1982). The diagonal elements should display two minima as the coordinate axes coincide with the principal directions of the 2-D earth. The off-diagonal elements should have just a single minimum. Vozoff (1972) shows that the principal axes orientation over 2-D structures is found directly by maximizing $|Z_{xy}|^2 + |Z_{yx}|^2$ with respect to θ . This same angle also minimizes $|Z_{xx}|^2 + |Z_{yy}|^2$. A combination of the first and third invariants in equation (2.21) gives another rotational invariant called the skew

$$S_1 = \frac{|Z_{xx} + Z_{yy}|}{|Z_{xy} - Z_{yx}|}$$

Combining the first and second invariants gives

$$S_2 = \frac{Z_{xx} + Z_{yy}}{Z_{xx}Z_{yy} - Z_{xy}Z_{yx}}$$

These have been used to assess the 2-D assumption. (Vozoff, 1972) since $S_1=S_2=0$ for any 1-D or 2-D earth.

Another symmetry property discussed by Fischer (1975) is that for 2-D models with a vertical plane of symmetry

$$\text{Arg}(Z_{xx}) = \text{Arg}(Z_{yy}) = \text{Arg}(Z_{xy}+Z_{yx})$$

where Arg is the principal value of the argument of the complex impedance. He states that this relationship as well as $S_1=0$ must hold above these types of structures.

2.5 Impedances from Magnetic Fields Alone

The OBM used for this study recorded only magnetic field components so that more information is required to calculate the MT impedances. That information (with a few approximations) is provided by the records of the Victoria

Geomagnetic Observatory (VIC). We assume that VIC is on the ocean surface directly above OBM and use the vertical gradient method described by Schmucker (1970), Poehls and von Herzen (1976) and Law and Greenhouse (1981). To find the impedance on the sea-floor using this technique we need to assume 1) the fields at the surface above OBM are adequately represented by the fields at VIC, 2) there are no magnetic fields induced by the homogeneous, isotropic ocean and 3) the structure below OBM and VIC is 1-D.

The first assumption, which transports VIC to above OBM, requires that the source fields remain uniform over the 350 km separating OBM from VIC. In addition, the difference between the oceanic and continental environments must not affect the fields significantly. Comparison of records from stations separated by several hundreds of kilometers reveals that the fields are indeed quite uniform over these distances. Chave et al (1981) give an approximate expression for the source field horizontal scale length which for the periods considered here is much larger than the OBM-VIC separation. Law and Greenhouse (1981) argue that the effects of changing source and conductivity structures counteract each other.

The second assumption of an immobile, uniform ocean is tenable at periods other than tidal periods. Larsen (1968) and Cox et al (1970) discuss EM fields induced by oceanic motions. There are several tidal spectral lines clustered around periods of 12 and 24 hours which are avoided in this analysis.

The third assumption, that of a 1-D structure, is never true but it must be made in order to derive an impedance from

magnetic fields alone. All the inversion techniques used here require a 1-D earth anyway, so the approximation is invoked sooner rather than later.

The magnetic fields measured at the two ocean levels are, from equation (2.6) ($\exp(+i\omega t)$, H-polarization),

$$H_y(0) = \frac{\gamma_1}{i\mu\omega} (A_1 e^{+\gamma_1 z_1} - B_1 e^{-\gamma_1 z_1}) e^{+i\omega t}$$

$$H_y(z_1) = \frac{\gamma_1}{i\mu\omega} (A_1 - B_1) e^{+i\omega t}$$

with $\gamma_1 = (1+i)(\mu\omega\sigma/2)^{1/2}$, $\sigma = 3.3$ S/m (an average for the ocean) and $z_1 = 2760$ m. Solving for the unknown constants yields

$$A_1 = \frac{i\mu\omega}{\gamma_1} e^{-i\omega t} \frac{(H_y(0) - H_y(z_1)e^{-\gamma_1 z_1})}{2\sinh \gamma_1 z_1}$$

$$B_1 = \frac{i\mu\omega}{\gamma_1} e^{-i\omega t} \frac{(H_y(0) - H_y(z_1)e^{+\gamma_1 z_1})}{2\sinh \gamma_1 z_1}$$

The sea-floor impedance from equation (2.7) is

$$Z_{xy}(z_1) = \frac{i\mu\omega A_1 + B_1}{\gamma_1 A_1 - B_1}$$

Therefore

$$Z_{xy}(z_1) = \frac{i\mu\omega \cosh \gamma_1 z_1 - 1/R_y}{\gamma_1 \sinh \gamma_1 z_1} \quad (2.22)$$

where $R_y = H_y(z_1)/H_y(0)$. For E-polarization and $\exp(+i\omega t)$

$$Z_{yx}(z_1) = + \frac{i\mu\omega \cosh \gamma_1 z_1 - 1/R_x}{\gamma_1 \sinh \gamma_1 z_1} \quad (2.23)$$

where $R_x = H_x(z_1)/H_x(0)$. For 1-D models we expect $Z_{xy} = -Z_{yx}$. Comparing equations (2.22) and (2.23) we see that this is true

since the horizontal magnetic components H_x and H_y are affected in exactly the same way over 1-D models as they diffuse from the sea-surface to the sea-floor. Thus, $R=R_x=R_y$.

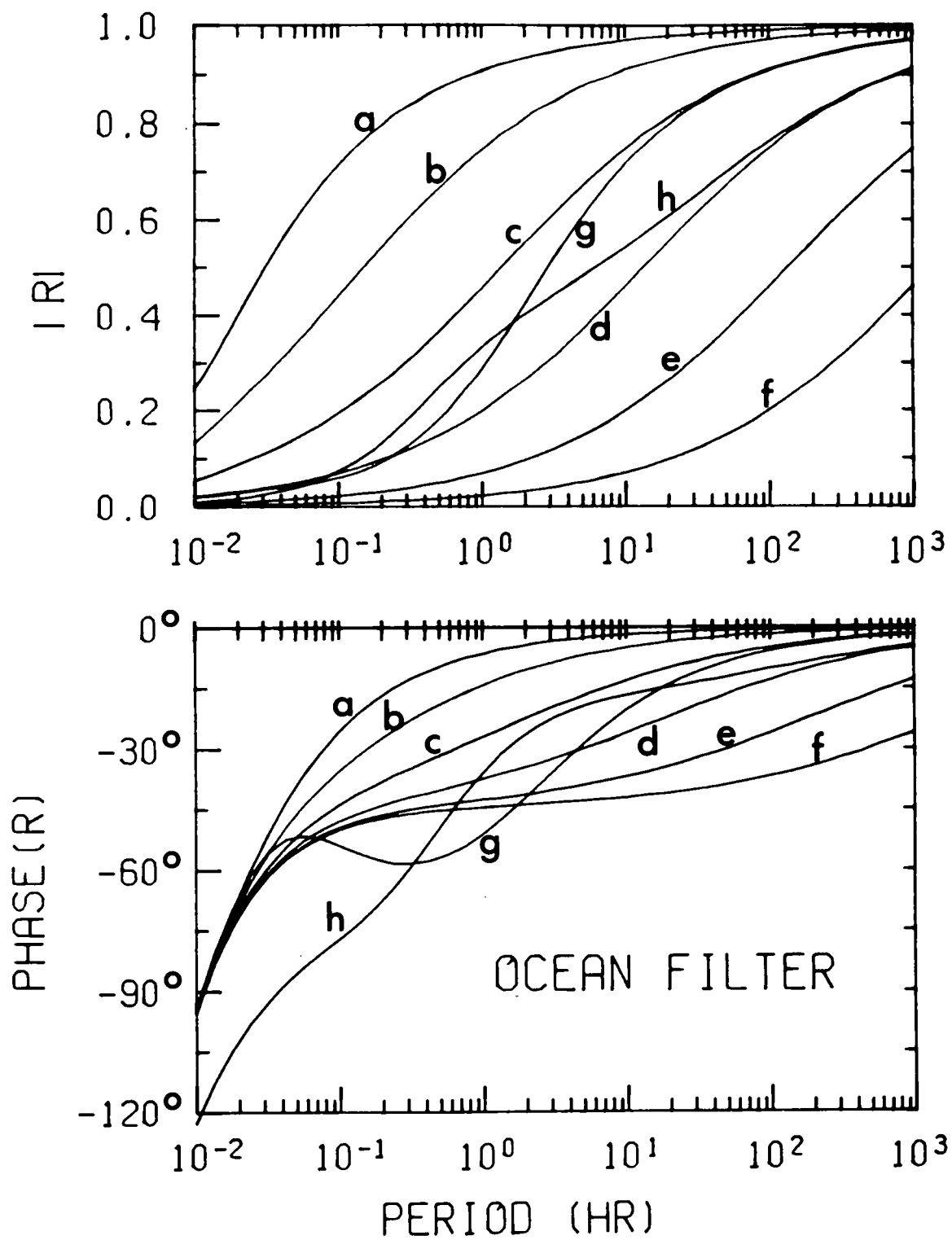
Because of the filtering effect of the ocean the OBM fields are attenuated and phase lagged with respect to VIC. This constrains $|R|$ to be less than unity and the phase of R , ϕ_R , to be less than zero degrees. Figure 7 shows $|R|$ and ϕ_R for an ocean with $\sigma=3.3$ S/m and $z_1=2760$ m above a range of earth structures. As the halfspace earth model becomes less conductive the attenuation of the fields between sea-surface and sea-floor increases (curves a through f). This is due to a destructive interference of the downgoing wave with the upgoing wave reflected from the sea bottom. The reflection coefficient

$$R_{12} = \frac{\sqrt{\sigma_1} - \sqrt{\sigma_2}}{\sqrt{\sigma_1} + \sqrt{\sigma_2}}$$

approaches unity as σ_2 approaches zero and so the net field in the ocean is very small. As the earth conductivity increases towards that of the ocean, R_{12} approaches zero and $|R|$ falls off with period according to the simple skin depth decay $\exp(-z_1/\delta)$ where $\delta=(2/\mu\omega\sigma_1)^{1/2}$. For $\sigma_2 > \sigma_1$ the reflection coefficient is negative and the incident and reflected waves interfere constructively to keep $|R|$ near unity over a broad range of periods. Two three layer models (curves g and h) have more variable $|R|$ curves but they still lie within intuitive bounds and approach the halfspace curves at short and long periods. In contrast, the ϕ_R functions for the multilayer earth models plotted in Figure 7B are more sensitive to the

Figure 7.

The ocean filter. The magnitude of the ratio R of a sea-floor magnetic field component to the corresponding sea-surface magnetic component is shown in A. The phase of this ratio is shown in B. All curves are calculated assuming an ocean thickness of 2670 m and conductivity $\sigma=3.3$ S/m. Curves a through f are derived from suboceanic halfspace models of conductivity 10, 1, 0.1, 0.01, 0.001 and 0.0001 S/m, respectively. Curve g results from a two layer over a halfspace suboceanic model with $\sigma_1=0.01$, $\sigma_2=0.001$, $\sigma_3=0.1$ S/m, $h_1=h_2=50$ km. Curve h is from a similar model with $\sigma_1=0.001$, $\sigma_2=0.1$, $\sigma_3=0.01$ S/m, $h_1=h_2=50$ km.



details of layering. the general trend, however, is that the phase lag increases as the suboceanic conductivity decreases.

2.6 Plane Wave Assumption

In this section we consider the validity of the plane wave approximation to the source fields. The most probable origin of the fields is in the highly conducting E-layer of the ionosphere at an altitude of about 110 km. The currents are not uniformly distributed around the earth but concentrated in auroral and equatorial electrojets. One model that tries to account for non-uniform source fields is that of a line current at some height h above a 1-D earth (Hermance and Peltier, 1970). Such a current flowing in the y direction leads to a generalization of one of equations (2.4) as

$$\partial^2 E_y / \partial x^2 + \partial^2 E_y / \partial z^2 = i \mu \omega \sigma(z) E_y$$

Assume $E_y(x,z) = X(x) Z(z)$ and use separation of variables to obtain

$$X(x) = A \cos(mx) + B \sin(mx)$$

$$Z(z) = C \exp(kz) + D \exp(-kz)$$

where $-m^2$ is the separation constant, $k^2 = (i \mu \omega \sigma(z) + m^2)$ and A , B , C , and D are constants. The electric field is

$$E_y(x,z) = [A \cos(mx) + B \sin(mx)][C \exp(kz) + D \exp(-kz)] \quad (2.24)$$

The horizontal magnetic field H_y is derived from this using one of the Maxwell equations (2.2). Note that for plane waves the horizontal wavenumber $m=0$ and equation (2.24) reduces to an expression similar to those in section 2.1. The total field at the earth's surface is formed by an appropriate superposition of solutions for all wavenumbers $0 < m < \infty$. If the

source model is generalized from a line current to a sheet current then Peltier and Hermance (1971) show how a linear combination of line current solutions is made to represent the sheet current distribution. These authors derive integral equations for the fields due to a sheet current with a Gaussian distribution 110 km above a 1-D earth. The standard deviation of the distribution is taken as 240 km. They find that the agreement between non-uniform and plane wave source impedances is affected by observer position and earth conductivity. We discuss these two parameters in turn.

Directly beneath the Gaussian electrojet the agreement is good, being generally within experimental error until periods greater than several hours. The plane wave approximation becomes worse as the observer moves laterally from under the electrojet. At a horizontal distance of 2.5 to 3 standard deviations the misfit reaches a maximum. Still larger distances reverse this trend and improve the agreement once again. The OBM site used in this study was located in the mid-latitudes (geomagnetic coordinates) perhaps 2000 km from the core of auroral electrojets and even further from equatorial electrojets. Therefore, on the basis of position, the plane wave approximation is valid.

The second factor influencing the accuracy of the plane wave approximation to the Gaussian electrojet source is the earth conductivity. Beneath this extended source there will be large deviations from plane wave theory when the earth is very resistive such as is found in continental areas. But the earth is expected to become very conductive at large depths because

of the high temperatures there. Peltier and Hermance (1971) show that for these types of models the agreement is much improved. For active, oceanic areas such as in our study the high temperatures and hence high conductivities are close to the surface. Therefore, on the basis of earth conductivity, the plane wave approximation is still reasonably valid.

2.7 Sphericity of the Earth

Plane waves propagating vertically downwards in a 1-D earth behave differently if the one dimension is changed from a Cartesian depth z to a spherical polar radius r . A discussion of the flat earth approximation is given by Kaufman and Keller, 1981, Chapter 6. They show that sphericity becomes important as the wavelength λ , or skin depth δ , of the field approaches the radius of the earth, a . Thus the impedances of the flat and spherical earth are very close when $a/\delta > 10$ where $\delta = \sqrt{\rho T / \mu \pi}$. Combining these approximate relations gives

$$\rho T < 445$$

for periods T in hours and an earth of constant resistivity ρ Ω -m. Periods up to 10 hours are acceptable if the major field attenuation occurs in a region with ρ of the order of 45 Ω -m. A rigorous analysis of the conversion from a spherical to a flat earth is given by Weidelt (1972). For the periods considered in this study an earth flattening transformation is not required.

CHAPTER 3 DATA REDUCTION

The methods of transforming the data to the frequency domain are examined in section 3.1. Once in the frequency domain the scalar and tensor transfer functions between the OBM and VIC horizontal fields are calculated (sections 3.2 and 3.3). Great care is taken to compute error bars that have a firm statistical basis. Winnowing criteria are proposed in section 3.4 to facilitate selection of the best possible data set. Finally, some details of the OBM analysis are presented (section 3.5).

3.1 Taking Transforms

A critical step in the analysis is to transform the high quality data of, for example, Figure 4 to equally high quality frequency domain data. The daily records are dominated by the S_q variation. Its effects are most pronounced near local noon and are minimal near local midnight when the induced currents are decaying very gradually. The S_q signal imposes constraints on the record length selected for transformation to the frequency domain. Since the fast Fourier transform assumes a periodic extension there should be no discontinuity between the initial and final time domain field values. If there is a jump, spurious frequencies will leak into the transform domain. To minimize the offset we break the record into multiples of 24 hours as in Figure 4. There are two advantages of segmenting the data in this way. Firstly, the tidal spectrum has many lines clustered around 12 and 24 hours. The energy in these lines can spread out into adjacent periods if

the record length is not an exact multiple of the tidal period. Data segments which are multiples of 24 hours will help minimize the spreading. A better plan would be to notch out all the known tidal lines or to remove them by a least squares fit to their known periods. Secondly, well-determined Fourier coefficients, with many degrees of freedom, are found by stacking the segment transforms as well as smoothing them with a spectral window.

The next step in the analysis seeks to remove any long period trends from the data and also to match the endpoints to reduce transform ringing. One alternative is to remove the mean and taper with a cosine bell typically of halfwidth ten percent of the series length. This method fails to deal with long period trends. Furthermore, tapering corresponds to a frequency domain convolution and any broad smoothing of the steep $1/f$ natural electromagnetic spectrum will overemphasize longer periods. A second alternative is to remove a least squares linear trend and taper. Because of the Sq waveform, such a trend removal often leaves the series with a larger endpoint offset than initially present. The third alternative is the one used in this analysis. A ramp between the first series point and the last is subtracted. This annihilates all wraparound offsets while at the same time removes a reasonable estimate of the long period trend. The method is faulty for segments which have rapid changes near their ends but because they all are chosen to begin near local midnight this is not a problem. Most ramps have slopes less than 1 nT/hr.

After the transforms are stacked they are smoothed with a

Parzen window. Properties of spectral windows are fully discussed by Jenkins and Watts (1968). The Parzen window is preferred over that of Bartlett or Tukey because it has small sidelobes and gives non-negative spectral estimates. The degrees of freedom (dof) for this window are $3.71T/M$ where T is the series duration and M is the time corresponding to the maximum lag of the time domain window.

Each Fourier coefficient begins with 2 dof, one each for its real and imaginary part. Smoothing with a Parzen window gives each estimate $3.71T/M$ dof. Stacking n segments results in a total of $3.71nT/M$ dof. Many degrees of freedom reduce the spectral estimate error but increase the bias. A balance must be found between these two competing effects to give accurate impedances close to their true values. Details of the choices made in this study are presented in section 3.5.

3.2 Scalar Ratio Estimates

As mentioned in section 2.5 the OBM recorded only magnetic field components. However, by taking the ratio of the OBM fields to those measured at VIC approximate MT impedances are found via the vertical gradient method. Without electric fields, then, we must put our effort into finding stable estimates for the once removed ratio R rather than finding the sea-floor impedance $Z(z_1)$ directly. Equations (2.22) and (2.23) are then used to give the impedance. Ratios are found from either scalar models such as considered in this section or from the tensor models of section 3.3.

The scalar model is

$$D(\omega) = R(\omega) Y(\omega) + e_1(\omega)$$

$$H(\omega) = R(\omega) X(\omega) + e_2(\omega)$$

where $D(\omega)$ and $H(\omega)$ are the horizontal fields at OBM, $Y(\omega)$ and $X(\omega)$ are the corresponding fields at VIC, $e_1(\omega)$ and $e_2(\omega)$ are white noise errors and $R(\omega)$ is the transfer function to be found. A straightforward estimate of $R = D/Y$ suffers severely from widely varying Fourier coefficients and the errors e_1 . A better estimate is found by assuming R is constant over a band of adjacent periods and from day to day at a single period. Then there are many equations for a single complex number R . Several solutions are possible. For instance, considering only the east-west fields, we write

$$R_1 = \frac{\langle DD^* \rangle}{\langle YD^* \rangle} \quad R_2 = \frac{\langle DY^* \rangle}{\langle YY^* \rangle} \quad |R_3| = \sqrt{\frac{\langle DD^* \rangle}{\langle YY^* \rangle}}$$

$$R_4 = \frac{\langle D \rangle}{\langle Y \rangle} \quad R_5 = \langle D/Y \rangle$$

where $\langle \rangle$ indicates an average over days and/or periods and $*$ indicates a complex conjugate. Ratios R_4 and R_5 have been tested on synthetic examples and are not as stable as the others. They yield estimates of R further from the true value (bias) and undergo much more variation. R_1 and R_2 are complimentary since the first overestimates and the second underestimates R in the presence of incoherent noise. To show this write

$$D = D_s + D_n$$

$$Y = Y_s + Y_n$$

where the subscript s refers to the true signal and the subscript n refers to noise. Then

$$\begin{aligned}\langle DD^* \rangle &= \langle (D_s + D_n)(D_s^* + D_n^*) \rangle \\ &= \langle D_s D_s^* \rangle + \langle D_n D_n^* \rangle\end{aligned}$$

since $\langle D_s D_n^* \rangle = 0$ for incoherent noise D_n . Similarly,

$$\langle YY^* \rangle = \langle Y_s Y_s^* \rangle + \langle Y_n Y_n^* \rangle \quad \text{and}$$

$$\langle DY^* \rangle = \langle D_s Y_s^* \rangle$$

assuming D_n and Y_n are also incoherent. Therefore

$$R_1 = \frac{\langle DD^* \rangle}{\langle YD^* \rangle} = \frac{\langle D_s D_s^* \rangle + \langle D_n D_n^* \rangle}{\langle Y_s D_s^* \rangle} = \frac{\langle D_s D_s^* \rangle}{\langle Y_s D_s^* \rangle} \left[1 + \frac{\langle D_n D_n^* \rangle}{\langle D_s D_s^* \rangle} \right]$$

and

$$R_2 = \frac{\langle DY^* \rangle}{\langle YY^* \rangle} = \frac{\langle D_s Y_s^* \rangle}{\langle Y_s Y_s^* \rangle + \langle Y_n Y_n^* \rangle} = \frac{\langle D_s Y_s^* \rangle}{\langle Y_s Y_s^* \rangle} \left[1 + \frac{\langle Y_n Y_n^* \rangle}{\langle Y_s Y_s^* \rangle} \right]^{-1}$$

Thus, D noise power will bias R_1 upwards and Y noise power will bias R_2 downwards. Some sort of average of R_1 and R_2 would reduce the bias in the estimate. R_3 provides that average since it is the geometric mean of R_1 and R_2 . The phase of R_3 is obtained from the cross spectrum $\langle DY^* \rangle$ which is the phase of both R_1 and R_2 .

The errors in the scalar ratio estimates are found using the theory of frequency domain response functions described by Jenkins and Watts, 1968, p429 and Bendat and Piersol, 1971, p199. These authors show how the smoothed power spectrum of the noise may be written approximately as

$$\langle ee^* \rangle = \langle \hat{e} \hat{e}^* \rangle + \langle YY^* \rangle |\hat{R} - R|^2$$

where $\langle \hat{e} \hat{e}^* \rangle$ is the smoothed power spectrum of the residual noise

$$\hat{e} = D - \hat{R}Y$$

and $\hat{R} = \langle DY^* \rangle / \langle YY^* \rangle$ is the estimate of R which minimizes the l_2 -norm of \hat{e} . If the smoothing generates n degrees of freedom

and $e'e'^*$ represents the true noise power then

$$\frac{n\langle ee^* \rangle}{e'e'^*} = \frac{n\langle \hat{e}\hat{e}^* \rangle}{e'e'^*} + \frac{n\langle YY^* \rangle}{e'e'^*} |\hat{R}-R|^2$$

is distributed as chi-squared with n degrees of freedom. Hence, by the additive property of x^2 variables the two statistically independent terms on the right hand side of the previous equation are distributed as x^2 with degrees of freedom that sum to n . The first term on the right is only different from the term on the left in that it is based on \hat{e} instead of e . Two additional constraints are placed on \hat{e} , one each by the real and imaginary part of \hat{R} . Therefore, the first term on the right is distributed as x^2_{n-2} . This leaves the second term on the right distributed as x^2_2 . The F-distribution governs the ratio of two x^2 variables with

$$\frac{x^2_1/n_1}{x^2_2/n_2}$$

distributed as F_{n_1, n_2} . Therefore,

$$\frac{n-2}{2} \frac{\langle YY^* \rangle}{\langle \hat{e}\hat{e}^* \rangle} |\hat{R}-R|^2$$

is distributed as $F_{2, n-2}$. Since

$$\begin{aligned} \langle \hat{e}\hat{e}^* \rangle &= \langle (D-\hat{R}Y)(D^*-\hat{R}^*Y^*) \rangle \\ &= \langle DD^* \rangle (1 - \gamma^2 DY) \end{aligned}$$

where the squared coherence

$$\gamma^2 DY = \frac{\langle DY^* \rangle \langle YD^* \rangle}{\langle DD^* \rangle \langle YY^* \rangle}$$

we write

$$\frac{n-2}{2} \frac{\langle YY^* \rangle}{\langle DD^* \rangle} \frac{|\hat{R}-R|^2}{(1-\gamma^2 DY)}$$

is distributed as $F_{2, n-2}$. The $(1-\delta)$ confidence interval for the transfer function R is then

$$|\hat{R}-R|^2 \leq \frac{2}{n-2} (1-\gamma^2 DY) \frac{\langle DD^* \rangle}{\langle YY^* \rangle} f_{2, n-2}(1-\delta) = k^2$$

where $f_{2, n-2}(1-\delta)$ is the 100(1- δ) percentage point of an F-distribution with 2 and $n-2$ degrees of freedom. Individual $|R|$ and ϕR confidence intervals are approximated by (Jenkins and Watts, 1968, p434)

$$| |\hat{R}| - |R| | \leq k$$

$$\sin|\phi\hat{R} - \phi R| \leq k/|\hat{R}|.$$

3.3 Tensor Ratio Estimates

The scalar ratio model assumes that there is no correlation between D and X or H and Y . This is never quite true. The tensor ratio model allows more general field relationships of the form

$$D(\omega) = R_{11}(\omega) Y(\omega) + R_{12}(\omega) X(\omega) + e_1(\omega)$$

$$H(\omega) = R_{21}(\omega) Y(\omega) + R_{22}(\omega) X(\omega) + e_2(\omega) \quad (3.1)$$

Consider only the first equation involving the east-west OBM field. Assuming that the transfer functions are constant over adjacent periods and from day to day at a single period we write

$$D_j = R_{11}Y_j + R_{12}X_j + e_j$$

$j=1, \dots, N$ days and/or periods. We need the many days and periods to determine the two unknown parameters R_{11} and R_{12} because otherwise there is just one equation in two unknowns. Therefore, this is now an overdetermined parametric linear inverse problem. In matrix form the preceding equation

becomes

$$\underline{D} = \underline{A} \underline{R} + \underline{e}$$

where $\underline{D} = (D_1, D_2, \dots, D_N)^T$, $\underline{R} = (R_{11}, R_{12})$, $\underline{e} = (e_1, e_2, \dots, e_N)^T$ and

$$\underline{A} = \begin{pmatrix} Y_1 & X_1 \\ Y_2 & X_2 \\ \vdots & \vdots \\ Y_N & X_N \end{pmatrix}$$

We want our parameter \underline{R} to minimize the l_2 -norm error $||\underline{e}||^2$.

Let \dagger denote the complex conjugate transpose.

$$\begin{aligned} ||\underline{e}||^2 &= \underline{e}^\dagger \underline{e} = (\underline{D} - \underline{A}\underline{R})^\dagger (\underline{D} - \underline{A}\underline{R}) \\ &= \underline{D}^\dagger \underline{D} - \underline{R}^\dagger \underline{A}^\dagger \underline{D} - \underline{D}^\dagger \underline{A}\underline{R} + \underline{R}^\dagger \underline{A}^\dagger \underline{A}\underline{R} \end{aligned}$$

The minimum occurs when $\underline{A}^\dagger \underline{A}\underline{R} = \underline{A}^\dagger \underline{D}$. These are called the normal equations. The corresponding least squares parameter estimate is

$$\underline{R} = (\underline{A}^\dagger \underline{A})^{-1} \underline{A}^\dagger \underline{D}$$

which is also known in inverse theory as the smallest model.

Written in full the normal equations are

$$\begin{pmatrix} \langle YY^* \rangle & \langle XY^* \rangle \\ \langle YX^* \rangle & \langle XX^* \rangle \end{pmatrix} \begin{pmatrix} R_{11} \\ R_{12} \end{pmatrix} = \begin{pmatrix} \langle DY^* \rangle \\ \langle DX^* \rangle \end{pmatrix}$$

and the parameter estimates are

$$\begin{aligned} R_{11} &= \frac{\langle DY^* \rangle \langle XX^* \rangle - \langle DX^* \rangle \langle XY^* \rangle}{\langle YY^* \rangle \langle XX^* \rangle - \langle YX^* \rangle \langle XY^* \rangle} \\ R_{12} &= \frac{\langle YY^* \rangle \langle DX^* \rangle - \langle YX^* \rangle \langle DY^* \rangle}{\langle YY^* \rangle \langle XX^* \rangle - \langle YX^* \rangle \langle XY^* \rangle} \end{aligned} \quad (3.2)$$

For the north-south OBM field we have

$$\begin{aligned} R_{21} &= \frac{\langle HY^* \rangle \langle XX^* \rangle - \langle HX^* \rangle \langle XY^* \rangle}{\langle YY^* \rangle \langle XX^* \rangle - \langle YX^* \rangle \langle XY^* \rangle} \\ R_{22} &= \frac{\langle YY^* \rangle \langle HX^* \rangle - \langle YX^* \rangle \langle HY^* \rangle}{\langle YY^* \rangle \langle XX^* \rangle - \langle YX^* \rangle \langle XY^* \rangle} \end{aligned} \quad (3.3)$$

Confidence intervals for the pair of parameters R_{11} and R_{12} or R_{22} and R_{21} can be found using the same method as for scalar ratios. However, this technique solves for the joint confidence limits of all the parameters. Pedersen (1982) takes a different approach and derives confidence intervals for each parameter separately. He shows how small deviations from the least squares solution \underline{R} result in a change in the value of $Q = ||\underline{e}||^2$ from its minimum Q_0 . The ratio $(n-4)(Q-Q_0)/Q_0$ is distributed as $F_{1, n-4}$. The confidence intervals for the real and imaginary parts of R_{11} are equal and equal to

$$\text{sqrt}\left[\frac{1}{n-4} \frac{1-\gamma^2 D.YX \langle DD^* \rangle}{1-\gamma^2 YX \langle YY^* \rangle} f_{1, n-4}(1-\delta)\right] = k_1 \quad (3.4)$$

and for the limits on the real and imaginary parts of R_{12} we have

$$\text{sqrt}\left[\frac{1}{n-4} \frac{1-\gamma^2 D.YX \langle DD^* \rangle}{1-\gamma^2 YX \langle XX^* \rangle} f_{1, n-4}(1-\delta)\right] = k_2 \quad (3.5)$$

where $f_{1, n-4}(1-\delta)$ is the 100(1- δ) percentage point of the F-distribution with 1 and $n-4$ degrees of freedom, $\gamma^2 YX$ is the squared coherence of the VIC horizontal field and

$$\gamma^2 D.YX = \frac{\langle YY^* \rangle \langle DX^* \rangle^2 + \langle XX^* \rangle \langle DY^* \rangle^2 - 2\text{Re}[\langle XY^* \rangle \langle DX^* \rangle \langle YD^* \rangle]}{\langle DD^* \rangle (\langle YY^* \rangle \langle XX^* \rangle - |\langle YX^* \rangle|^2)}$$

is the multiple squared coherence of the OBM D channel on the horizontal VIC channels. Approximate confidence intervals for the magnitude and phase are

$$\begin{aligned} | |\hat{R}_{11}| - |R_{11}| | &\leq k_1 \\ | |\hat{R}_{12}| - |R_{12}| | &\leq k_2 \\ \sin|\phi \hat{R}_{11} - \phi R_{11}| &\leq k_1 / |\hat{R}_{11}| \\ \sin|\phi \hat{R}_{12} - \phi R_{12}| &\leq k_2 / |\hat{R}_{12}| \end{aligned}$$

with similar expressions for the confidence limits of R_{22} and R_{21} .

3.4 Winnowing Ratio Estimates

Calculating scalar or tensor ratios as described in the preceeding two sections generates several hundred complex numbers all vying for the attention of the interpreter and hoping for promotion to sea-floor impedances for use in model construction. Only a few ratio estimates are required at periods spaced roughly logarithmically. This section describes some criteria used to extract the best possible data set which must be compatible with the assumptions made concerning the source fields and the earth. An interactive computer programme was written to apply any combination of the winnowing criteria with any rejection level to the vast number of $R(\omega)$. The algorithm acts like the sieve of Erasthones to allow a few prime candidates to fall through the mesh and be used for model construction.

3.4.1 Ocean Filter

As demonstrated in section 2.5 and Figure 7 the ocean filter attenuates and phase lags OBM fields with respect to those at VIC. These effects require $|R| < 1$ and $\phi R < 0^\circ$. For periods $T < 0.1$ hr the attenuation is severe and so estimates may fall prey to noise. Also these periods are liable to be influenced by near-surface inhomogeneities. Hence, a short period cutoff of $T = 0.1$ hr is established. With $T > 0.1$ hr and plausible suboceanic models a further rough limit on the phase

of R is set as

$$-90^\circ < \phi_R < 0^\circ$$

3.4.2 Vertical Field

For a 1-D earth and plane incident EM waves the vertical field is identically zero. Over 2-D models the vertical field is a linear combination of the horizontal fields. To avoid contradicting our 1-D assumption we select periods at which the vertical field is relatively small and incoherent with respect to the horizontal fields. That is, we require

$$\frac{\langle ZZ^* \rangle}{\langle DD^* \rangle} \ll 1 \quad \frac{\langle ZZ^* \rangle}{\langle HH^* \rangle} \ll 1 \quad \text{and} \quad \gamma^2 Z.DH \ll 1$$

where Z is the vertical OBM field and $\gamma^2 Z.DH$ is the multiple squared coherence of Z on D and H . These conditions are similar to requiring that the tipper, as described by Vozoff (1972), be small and highly variable.

3.4.3 Ratio Errors

To constrain the conductivity models as much as possible we select ratio estimates with small errors. The confidence limit formulae for tensor ratios, equations (3.4) and (3.5), show that small ratio errors result from $\gamma^2 D.YX$ and $\gamma^2 H.YX$ near unity. High coherencies occur when the model in equation (3.1) is a good description of the true situation at a particular period with very little residual incoherent noise. In addition, $\gamma^2 YX$ must be small. If it is not then not only do the errors become large but the denominator in the expressions for R_{ij} in equations (3.2) and (3.3) approaches zero and leads

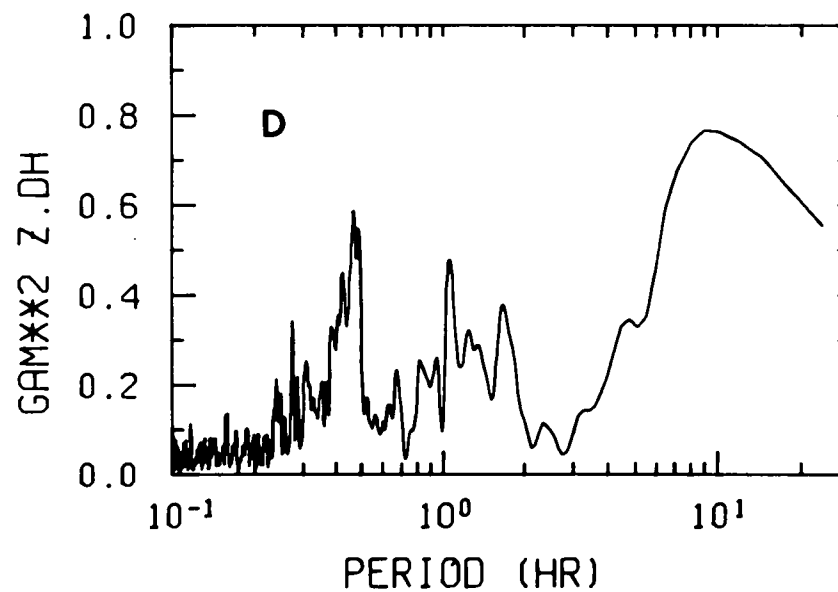
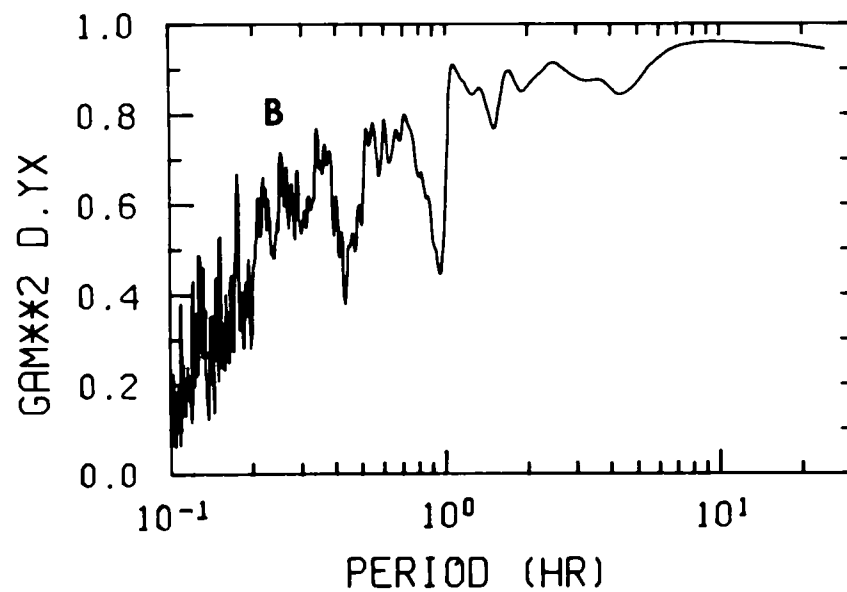
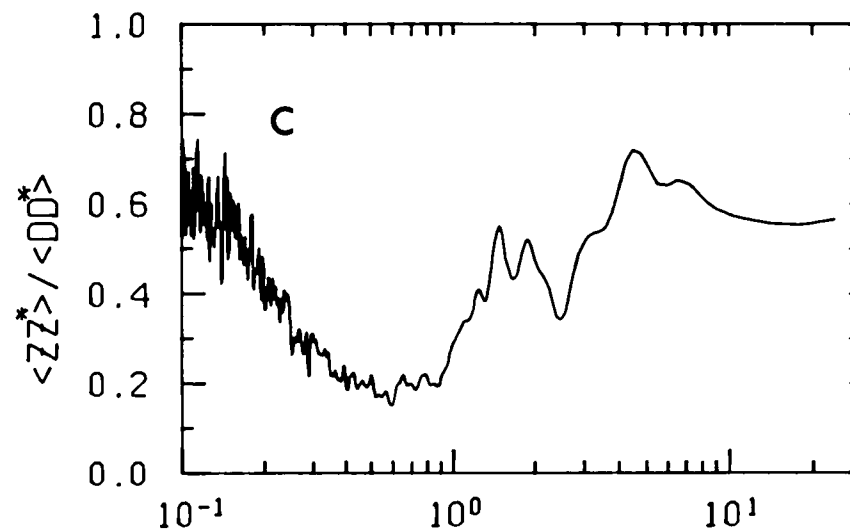
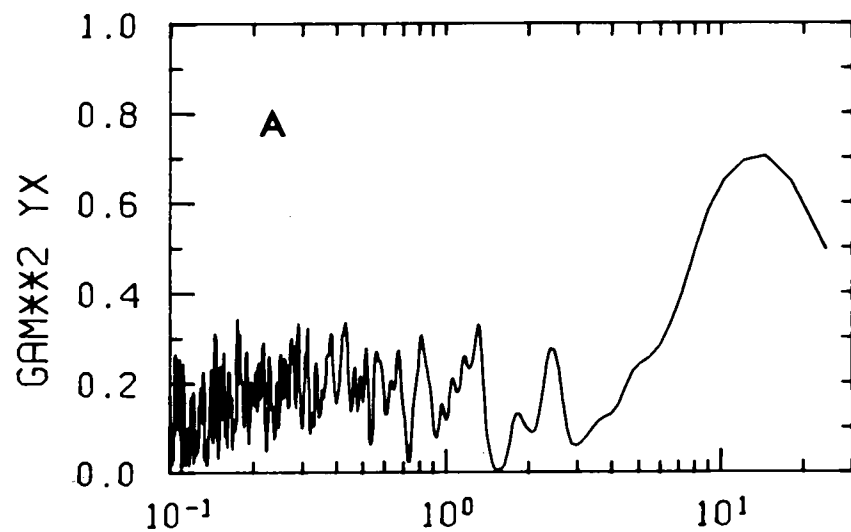
to very biased estimates.

3.4.4 Dispersion Relations and Inequalities

Weidelt (1972) and Fischer and Schnegg (1980) describe dispersion relations and inequalities between apparent resistivities and phases which must be satisfied over 1-D models. These constraints are not immediately applicable since they require a large number of accurately known responses. This is definitely not the case for practical MT data. Linear inverse theory which is designed to operate with a finite number of inaccurate data could be used to predict a phase curve from a more reliably determined apparent resistivity curve or vice versa. This approach was not used here.

Figure 8 shows some of the winnowing criteria as functions of period. Graph A is the squared coherency of the VIC horizontal field, $\gamma^2 YX$. At periods near 10 hours the curve surges up to very high values. Ratios calculated near here will be heavily biased upwards and will have large errors. Graph B is the multiple squared coherence of an OBM channel on the VIC horizontal channels, $\gamma^2 D.YX$. This curve should be near unity. Two deep notches at one half and one hour period plus a fall off at very short periods indicate regions to avoid. Graph C plots the relative magnitude of the OBM vertical field $\langle ZZ^* \rangle / \langle DD^* \rangle$ and suggests a rather narrow range of acceptable periods. Graph D shows the coherency between the OBM vertical and horizontal channels, $\gamma^2 Z.DH$. Again periods near one half, one and ten hours should be avoided.

Figure 8.
Winnowing criteria as functions of period. The squared coherence of the horizontal VIC field is shown in A. The multiple squared coherence of the OBM D channel on the VIC horizontal channels is shown in B. The magnitude of the vertical OBM field relative to one of its horizontal fields is shown in C. The multiple squared coherency between the OBM vertical and horizontal channels is shown in D. All curves are calculated from spectra with 136 degrees of freedom.



3.5 OBM Data Reduction

This section describes some specific details of the OBM data analysis up to the selection of apparent resistivity and phase data for use in model construction.

First of all, the relative magnitudes of the OBM horizontal field components during magnetically quiet times are used to rotate the data into the geomagnetic coordinate system (the same as at VIC). The rotation angle is 20.6° clockwise.

Following the discussion of section 3.1 the total record is broken up into multiples of 24 hours. Several different data groupings are used. Many degrees of freedom are possible when 33 one-day segments are stacked and smoothed. However, a better selection of longer period Fourier coefficients which avoid the major tidal harmonics at 4, 6, 8, 12 and 24 hr is provided by stacking segments of, say, 72 hours duration. For this study 31 one-day, 16 two-day, 11 three-day, 8 four-day, 4 eight-day and 3 eleven-day non-overlapping segments are selected for analysis. The transforms within each group are stacked and smoothed by a Parzen window with $T/M=2.5, 2.5, 3.3, 4, 5$ and 5 respectively. The resulting degrees of freedom are 287, 148, 136, 119, 74 and 56 respectively. Smoothed tensor ratios calculated from these different data groupings are similar. Periods where they disagree dramatically are avoided. Ratio estimates at shorter periods are selected from the one-day stack since it has the most degrees of freedom. Above $T=3$ hr the choice becomes very limited so estimates are selected from the two-day grouping, and so on. All choices are

made on the basis of the winnowing criteria outlined in section 3.4. At periods greater than 7 hr ratios from any grouping have difficulty passing the winnowing tests. When standards are relaxed impedances derived from these longer period responses, particularly the phases, are badly misfit by the modelling routines. Hence, the maximum period is reluctantly taken to be $T=5.5$ hours.

The tensor ratio estimates are rotated into the reference frame which maximizes the diagonal elements (R_{11} and R_{22}) at the expense of the off-diagonal elements (R_{12} and R_{21}) following the procedure of Everett and Hyndman (1967) and Banks (1973).

Confidence limits found for the unrotated diagonal elements are used for the rotated diagonal elements. Impedances are calculated using equation (2.22). The errors in the magnitude and phase of the impedance are derived from a brute force method. The ratios R are perturbed by Gaussian noise and the variance of the resulting (assumed Gaussian) distribution of impedances is calculated.

The east-west OBM field gives impedances Z_{xy} which pass the winnowing criteria and are successfully modelled by all the 1-D inversion schemes. On the other hand, the north-south OBM field produces unstable Z_{yx} estimates which are not well fit. Hence, only Z_{xy} is used for model construction. It was expected that the reverse would be true since Z_{yx} values are based on magnetic fields perpendicular to the strike of the very two dimensional continental slope. Electric fields are then along strike and the apparent resistivities are less

susceptible to errors (Vozoff, 1972). However, all apparent resistivities are very low whether they are derived from Z_{xy} or Z_{yx} or the scalar transfer function analysis.

The final data with one standard deviation error bars are presented in Figure 9. The apparent resistivities of Figure 9A are calculated from $\rho_a = |Z_{xy}|^2 / \mu \omega$. They all are surprisingly small, lying between 5 and 10 $\Omega\text{-m}$ ($\sigma = 0.2$ and 0.1 S/m). Different conventions and MT response functions require the phases to be in different quadrants. For convenience, they are plotted in Figure 9B in the first quadrant which is equivalent to the lead of the electric over the magnetic field. A phase less than 45° implies a more resistive substratum while a phase greater than 45° suggests a more conductive substratum.

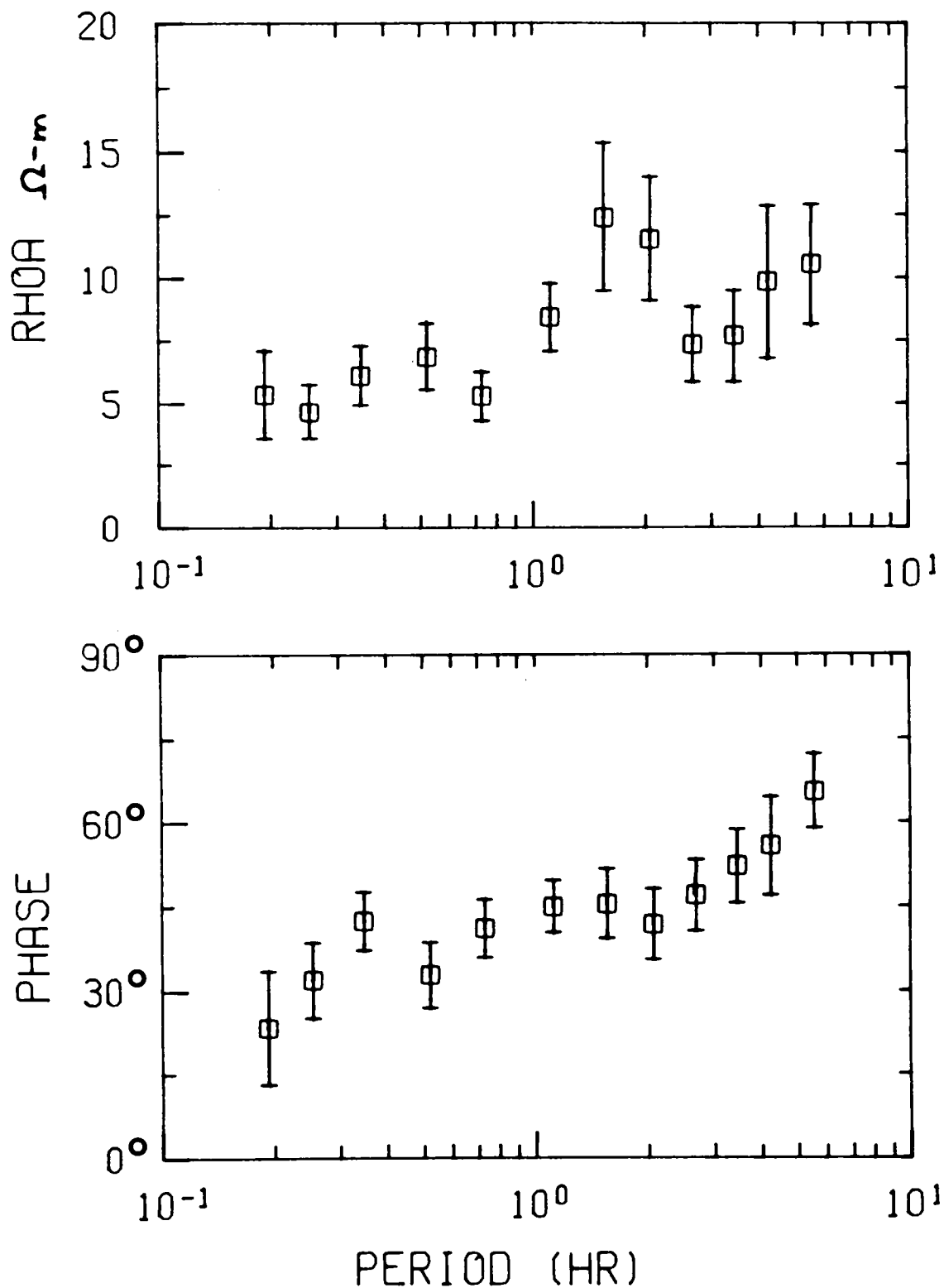


Figure 9.
The final data calculated from the vertical gradient method impedances. Apparent resistivities are shown in A while the phases are shown in B. The phase can lie in any quadrant and is plotted here in the first, for convenience.

CHAPTER 4 INVERSION OF IMPEDANCES FOR CONDUCTIVITY

The limited number of imprecise data shown in Figure 9 do not uniquely specify a particular conductivity versus depth profile. Non-uniqueness is a difficulty common to all geophysical data sets. It is especially acute for the non-linear MT analysis since no theory yet exists to assess the non-uniqueness in a similar manner that unique Backus-Gilbert averages quantify linear inverse problems (Backus and Gilbert, 1970). One way of grappling with non-uniqueness is to use the data to construct some of the infinitely many acceptable conductivity models. By using different inversion algorithms it is hoped that most dark corners of model space will be illuminated and that no other significantly different models will exist which satisfy the data to within their errors.

One inversion routine (section 4.1) constructs models composed of delta functions of conductance. Such models are geophysically unreasonable but fit the data more precisely than any other model type. If this minimum misfit is still unacceptably large then the data set is incompatible with the 1-D assumption and new responses must be found. This programme acts as a global winnowing criterion which rejects entire data sets. In a manner similar to other inversion routines it can also identify spurious, badly determined responses even though the misfit error is distributed throughout the data.

Four inversion routines used here generate intuitively satisfying simple models. Simple is defined as either a small number of constant conductivity layers (section 4.2) or a smoothly varying continuous conductivity function (section

4.3). The first definition is expected to apply near the surface where discontinuities are more likely to occur. The second definition is more applicable to the deep earth structure where changes are more gradual. The final routine (section 4.4) attempts to quantify the non-uniqueness allowed by the data by finding models which maximize or minimize the integrated conductivity between specified depths. Thus, global bounds on the average conductivity or on the conductance are calculated.

The misfit criterion we use is based on the chi-squared distribution

$$x^2 = \sum_{j=1}^N |c_j - c(\omega_j)|^2 / s_j$$

where c_j is a dummy variable representing the measured response at ω_j , $c(\omega_j)$ is the response calculated from the constructed model, s_j is the standard deviation of c_j and N is twice the number of periods since at each period we can have c_j in real and imaginary parts or as magnitudes and phases. In practice, the difference in the x^2 misfit is small for different representations of the MT response (complex impedances, apparent resistivities and phases). We make the hypothesis that the constructed model accurately represents the real earth structure. Even when this assumption is true x^2 does not equal zero because of random errors in the data, c_j . In fact, the expected value of x^2 is N . Large values of $x^2 \gg N$ or small values of $x^2 \ll N$ have a low probability of resulting merely from random misfit errors to the data points. Therefore, for x^2 in these ranges we must reject our original hypothesis of model and true earth equivalence. Hence, we

define acceptable models as those which have χ^2 within the (approximate) 95 percent confidence interval

$$N - 2\sqrt{2N} \leq \chi^2 \leq N + 2\sqrt{2N}$$

4.1 Best Fitting Models

Parker (1980) and Parker and Whaler (1981) describe how D^+ models consisting of delta functions of conductance minimize the misfit to the data. D^+ models of the OBM data of 12 apparent resistivities and 12 phases have χ^2 equal to about 20. Hence the data set is compatible with the 1-D assumption and more geophysically reasonable models exist which fit the data.

4.2 Layered Models

4.2.1 A Layer over a Halfspace

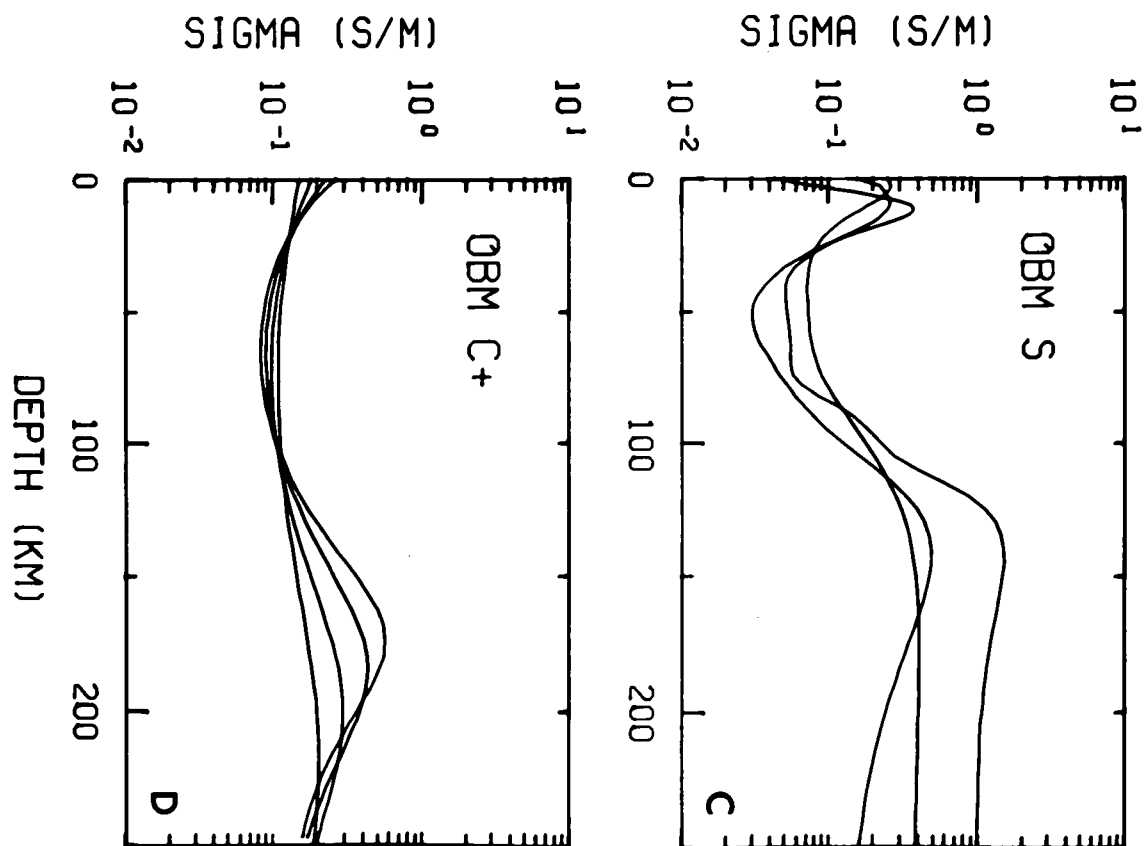
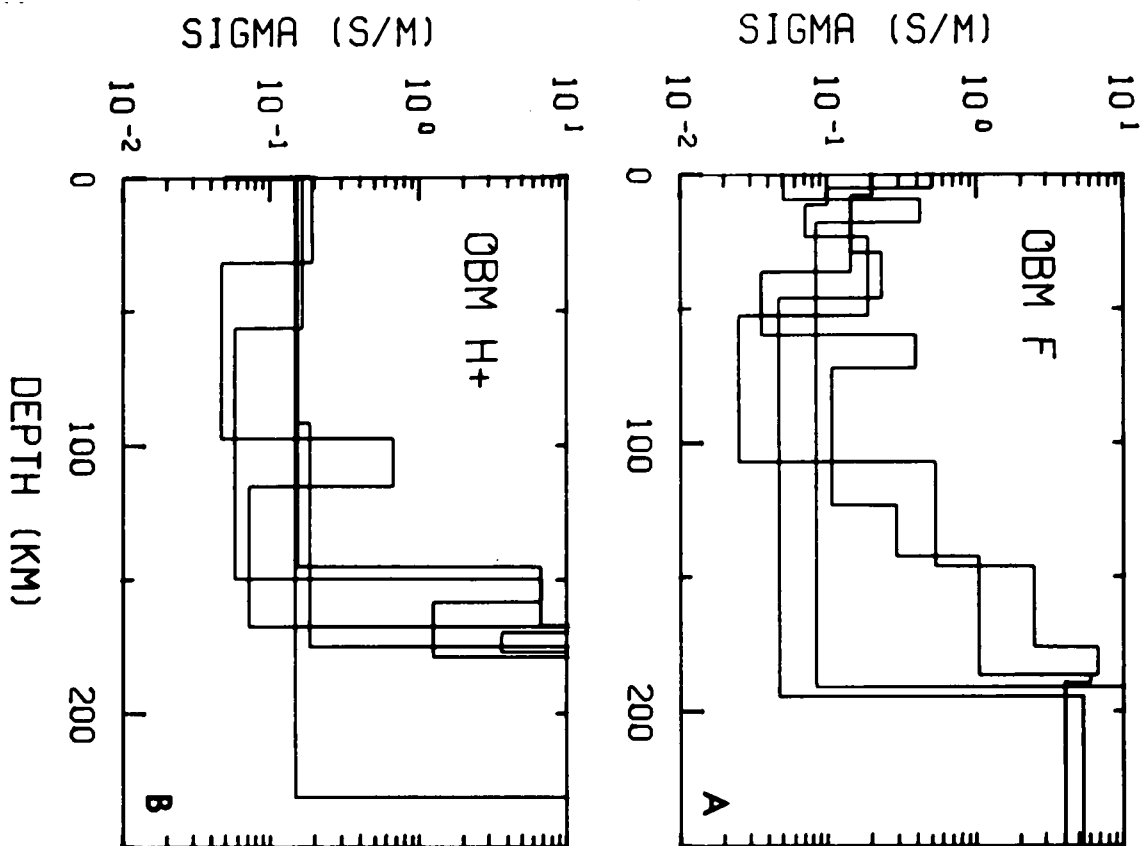
Fischer et al (1981) describe a technique for constructing layered conductivity models. The method is basically a repeated application of the layer over a halfspace impedance formula given by equation (2.14). The surface conductivity is a variable parameter. Once it is fixed the shortest period datum is used to find the thickness of the surface layer and the underlying conductivity assuming the second layer is a halfspace. The next longest period determines the thickness of the second layer and the conductivity of the third, and so on. If a period has a skin depth which is not greater than some factor times the model depth so far constructed then it is deleted and the next longest period tried. This test assures that the field has

penetrated significantly into the underlying structure and prevents generation of insignificant thin layers. All periods are used, however, in calculating the χ^2 misfit of the model to the data. Four such acceptable F models are shown in Figure 10A. While the details of the overlapping lines are obscured the general trend is clear. Surface conductivities are about 0.1 to 0.2 S/m and a more resistive zone is indicated between 50 and 100 km depth. Below this point the models vary a great deal. This fact as well as other arguments suggest that the data cannot resolve structures below about 120 km.

4.2.2 Constant $\mu\sigma h^2$ Layers

Parker (1980) and Parker and Whaler (1981) discuss what they term H^+ models which have constant $d^2 = \mu\sigma h^2$ layers. At the surface of such a model the MT responses may be written in terms of a partial fraction expansion. Parameters of the expansion are found which minimize the χ^2 misfit for a given d^2 . The layer conductivities and thicknesses are then found by recursion through an equivalent continued fraction representation, similar in form to equation (2.12). Small values of d^2 produce very thin, very high conductivity layers. In fact, as d^2 approaches zero the χ^2 misfit drops to the minimum found by D^+ and the layers become like delta functions. More reasonable values for d^2 yield models with thicker layers of more uniform conductivity. Five H^+ models are shown in Figure 10B. As with the F models, the surface conductivity is between 0.1 and 0.2 S/m and a resistive zone is indicated between 50 and 100 km depth. At depths below 120

Figure 10.
Acceptable conductivity models based on the data of Figure 9. F and H⁺ layered models are shown in A and B, respectively. S and C²⁺ smooth models are shown in C and D, respectively. Some curves fit the data more precisely than others but all have a χ^2 misfit less than 38 which is the upper limit of the 95 percent confidence interval.



km the conductivity varies by two orders of magnitude and is not to be believed.

4.3 Smooth Models

4.3.1 Linearized Inversion

Oldenburg (1979) describes a method of constructing smooth conductivity profiles. The non-linear MT equation is transformed into a linear equation relating small changes in the model to small changes in the responses. Smooth perturbations to a starting model are found which reduce the χ^2 misfit between the measured responses and those calculated from the new perturbed model. The process is repeated until convergence is attained, usually within 5 iterations. Three S models are shown in Figure 10C. Again, surface conductivities are near 0.1 to 0.2 S/m. There is some indication of a narrow region of increased conductivity near 10 km not present on models from other algorithms. The resistive zone between 50 and 100 km is still prominent. Below 120 km each profile returns to the conductivity of the halfspace starting model that generated it. Thus, the data are powerless to alter the structure below about 120 km. Further confirmation that the high conductivities at these depths are not justified by the data is provided by the following test. Oldenburg's algorithm can construct models from only apparent resistivities--phases are not required. Seventeen apparent resistivities at periods ranging from 0.2 to 27 hours are inverted. Without the long period phases models are found which fit the data. All the models have nearly uniform conductivities of 0.07 S/m with no

highly conductive regions at depth. Therefore, we do not believe structure below 120 km based on just the original 12 complex data.

4.3.2 Gel'fand-Levitan Inversion

Parker (1980) and Parker and Whaler (1981) discuss an inversion scheme based on the techniques of Gel'fand and Levitan (1955). As for H^+ models the responses are written as a partial fraction expansion. The spectral function of this expansion is manipulated by the Gel'fand-Levitan method to give another function which is part of a Schrodinger equation. This does not seem very progressive until it is discovered that the MT equation can be transformed into a Schrodinger equation. In this rather involved fashion, infinitely differentiable conductivity profiles are constructed. The surface conductivity, σ_0 , is the parameter for this algorithm. Large values of σ_0 produce small x^2 misfits and models which resemble smoothed delta functions. Small values of σ_0 increase the misfit error and give more uniform conductivity profiles. Four such C^{2+} profiles are shown in Figure 10D. Very little variation from σ_0 is present in the top 100 km. The curves diverge somewhat near 150 km but this has been shown to be beyond the depth of resolution of the data.

4.4 Conductance Bounds

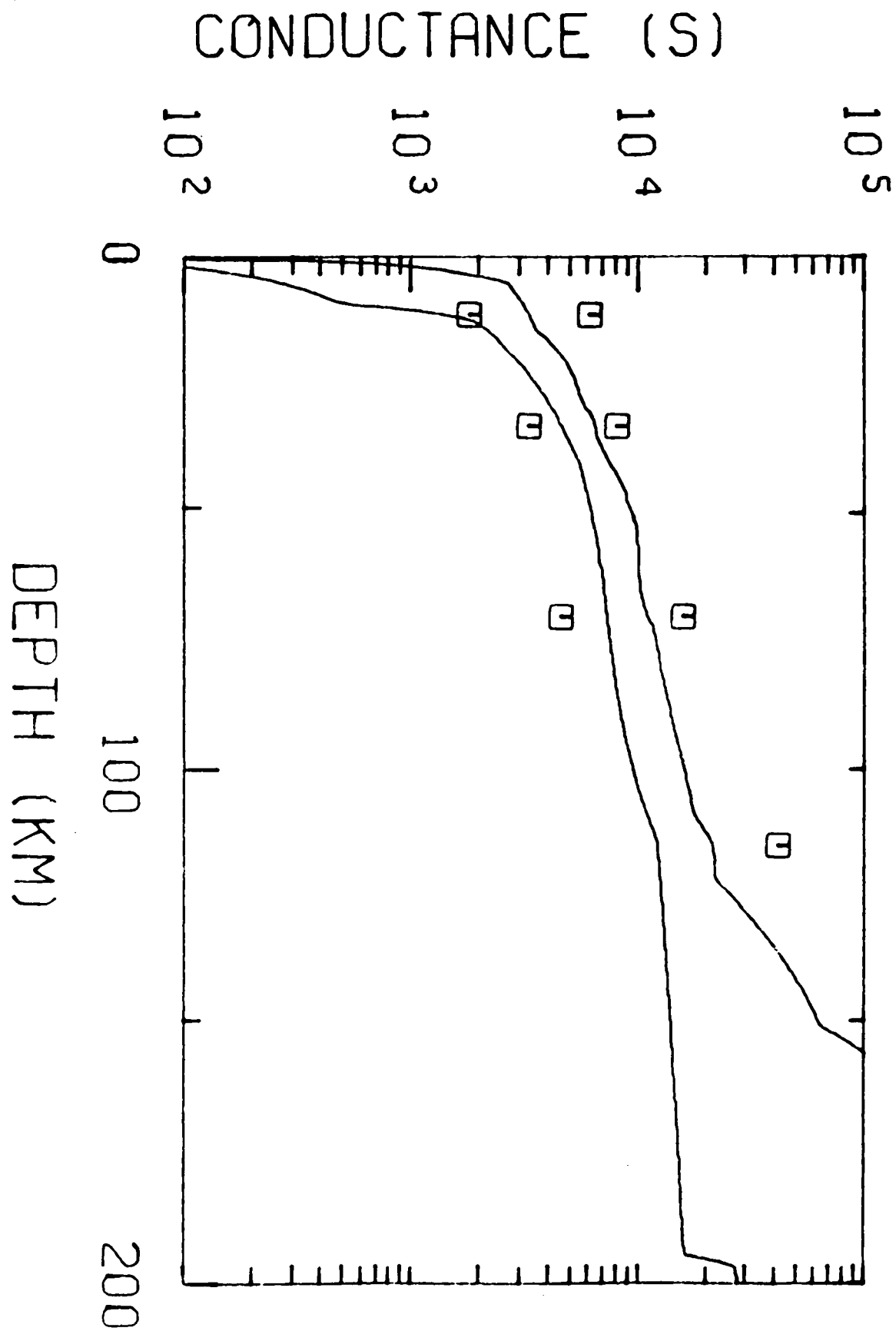
To summarize all the models from the four inversion algorithms the conductance curves are calculated. The conductance at a depth z is simply the integral of the

conductivity from the surface to level z . All sixteen conductivity profiles presented in Figure 10 are integrated in this way. At any particular depth the maximum and minimum conductance is noted and the resulting bound curves are plotted in Figure 11. True, global bounds which maximize and minimize the conductance at several depths are also shown. These points are found using the linear programming techniques described by Oldenburg (1983). As expected they lie outside the approximate curves calculated on the basis of just 16 different models. The approximation to the true bounds in Figure 11 is good down to a depth of about 80 km. The agreement implies that the conductances of the constructed models are representative of the true diversity of conductances permitted by the data in this region. The approximation breaks down at greater depths where the conductivity profiles, dissimilar though they are, fail to adequately explore the space of acceptable conductances. A minimum bound at a depth of 115 km was not found due to convergence problems. Indications were, however, that the bound point did not lie close to the approximate curve.

The conductance bound curves derived from either method indicate well and poorly defined regions. Where the bounds are close, the data have the power to constrain the total conductance down to that depth. Wide bounds, however, indicate where the data have less influence and admit large conductivity and conductance variations. The OBM conductance bounds are narrow down to about 50 km. Between 50 and 120 km they gradually increase as resolution decreases (note the

logarithmic scale). Underlying, extremely wide bounds confirm the earlier proposition that resolution is lost below 120 km.

Figure 11.
Conductance bounds. Approximate upper and lower bounds on the conductance calculated from the 16 acceptable models in Figure 10 are plotted as lines. True, global bounds at several depths are plotted as squares.



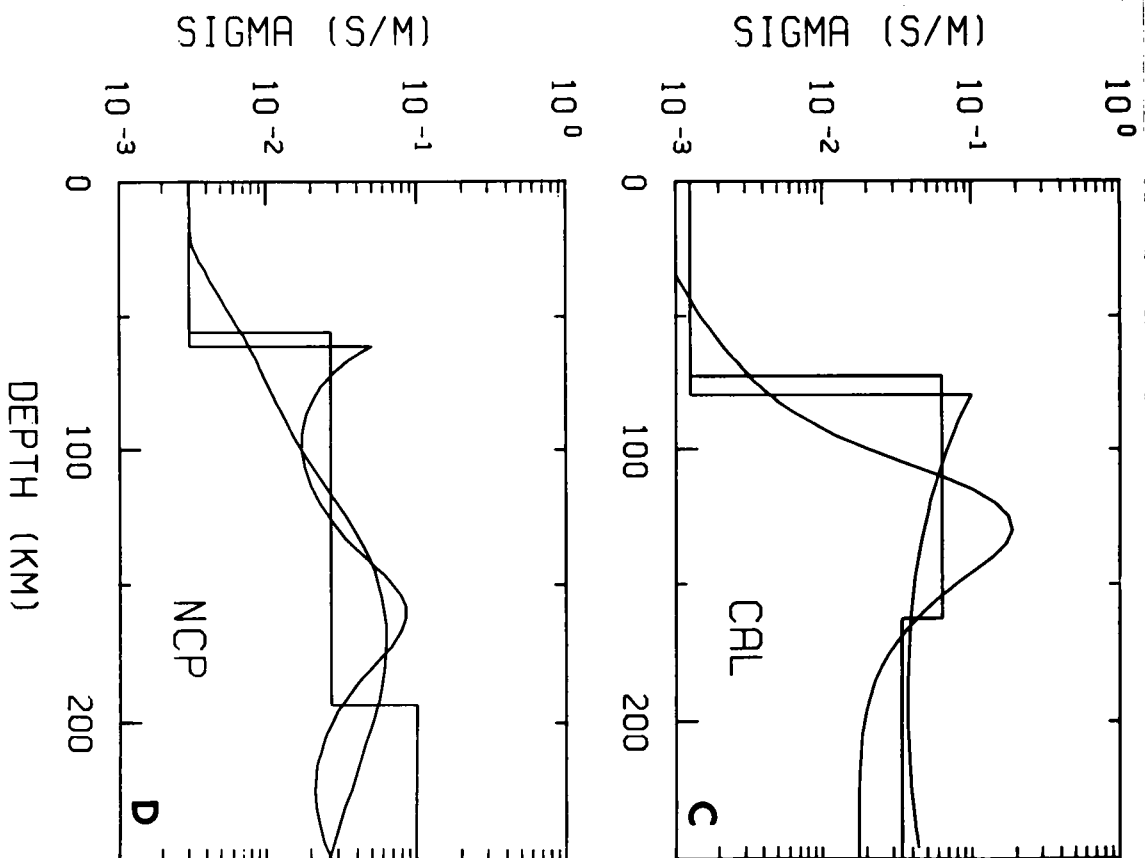
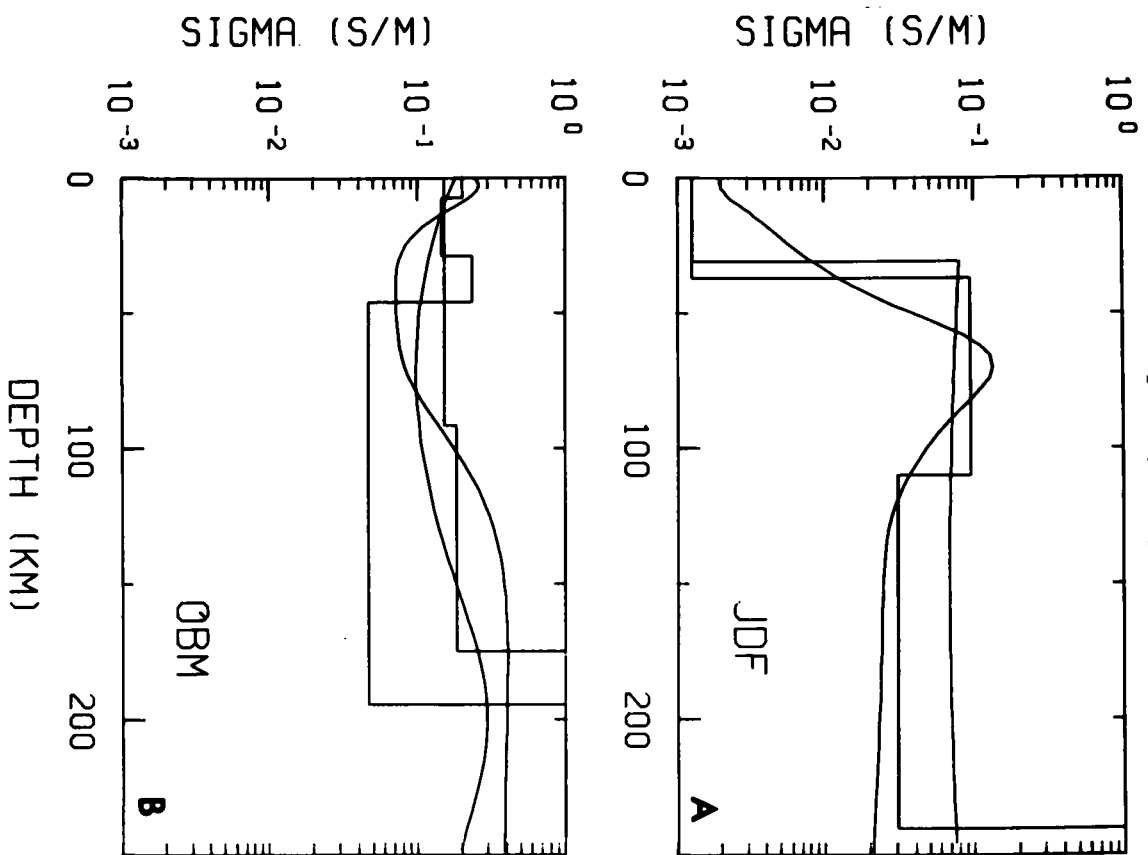
CHAPTER 5 CONCLUSIONS

5.1 OBM Results Compared with Other Studies

There are a growing number of ocean bottom MT analyses for sites on the Pacific plate. Three in particular have been amalgamated into a picture consistent with theories of sea-floor spreading. Oldenburg (1981) combined results from stations JDF, CAL and NCP above 1, 30 and 72 my old lithosphere, respectively. Several interesting trends were observed. Firstly, the distinct conductive zone visible in models for all three sites began at deeper depths as the lithospheric age increased. The sharp rise in conductivity was interpreted as the boundary between the cold, resistive lithosphere and the hot, conductive asthenosphere. An increase in depth with age is expected since the lithosphere thickens with age. Secondly, a partial melting interpretation of the conductivity high showed the melt fraction decreased with increasing age and was correlated with the seismic low velocity zone interpreted from Rayleigh wave dispersion data. These relationships suggest that the conductive zone is the core of a partially molten asthenosphere. Finally, temperatures, too, generally decreased with increasing age in accordance with a thickening lithosphere. A new analysis by Parker, Oldenburg and Whittall (1983) confirms that these trends exist but that they are not as strong as initially believed due to the surprisingly large non-uniqueness of the MT method. Therefore, an additional analysis on another age lithosphere would be most helpful in ratifying or refuting the general pattern outlined above. This was one of the

Figure 12.

Minimum structure conductivity models for four Pacific plate ocean bottom stations. From A through D the sites were above 1, 3, 30 and 72 my old lithosphere. The OBM models of 12B are clearly distinct from those of the other sites.



motivations for recording the OBM data on 3 my old lithosphere, an age intermediate between JDF and CAL.

Models constructed by different inversion schemes for all four stations are plotted in Figure 12. In the hope of capturing the essential earth features, models with a minimum of structure are selected from the infinity of acceptable profiles. Curves for JDF, CAL and NCP (Figures 12A, 12C, 12D) all have the same basic form. They are quite resistive near the surface and have a conductive zone beginning between 40 and 80 km. Below this depth some models indicate a decrease in conductivity while others maintain a fairly constant level. The OBM profiles are quite distinct (Figure 12B). They all have a roughly uniform conductivity centered on about 0.2 S/m until 120 km depth where resolution is lost. There are no major conductive or resistive zones such as are found for the other three sites.

To find the melt fraction and temperature profiles we use the pyrolite plus 0.1 percent water petrology of Ringwood (1975) as well as his $f(T,P)$ function which relates the melt fraction, f , to the temperature, T , and pressure, P . One further equation which expresses the minimum f in terms of the melt, solid and bulk conductivities is borrowed from Shankland and Waff (1977). Results for the OBM data are presented in Figure 13. Below the first few kilometers of sediments where the pyrolite petrology is expected to hold the melt fraction is about 0.12 (Figure 13B). This drops fairly smoothly to 0.03 by 120 km as less and less melt is required to account for the observed bulk conductivity. One model gives an extremely high

Figure 13.

A partial melting and temperature interpretation of the OBM minimum structure models. The minimum structure models from the four inversion routines are plotted in A. The minimum percentages of melt required to account for the observed bulk rock conductivities are shown in B. The corresponding temperature profiles are shown in C.

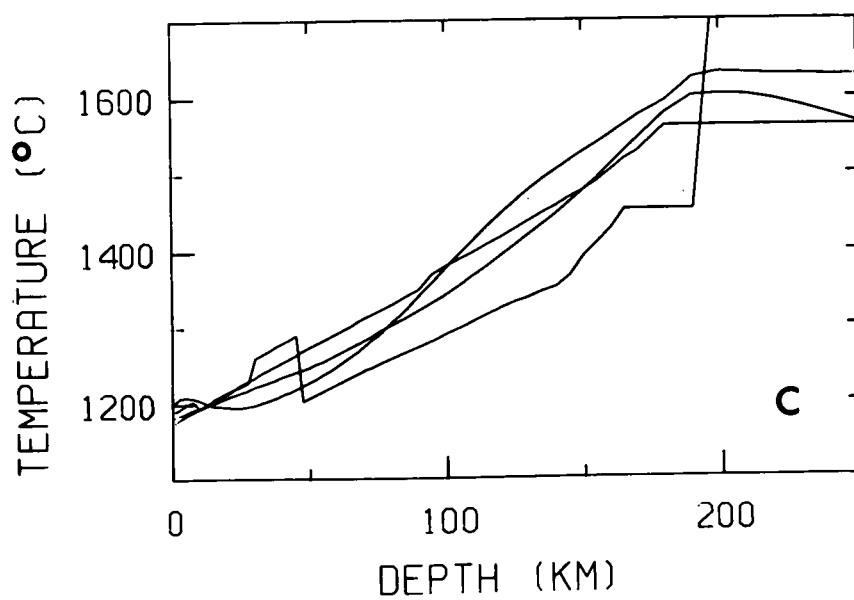
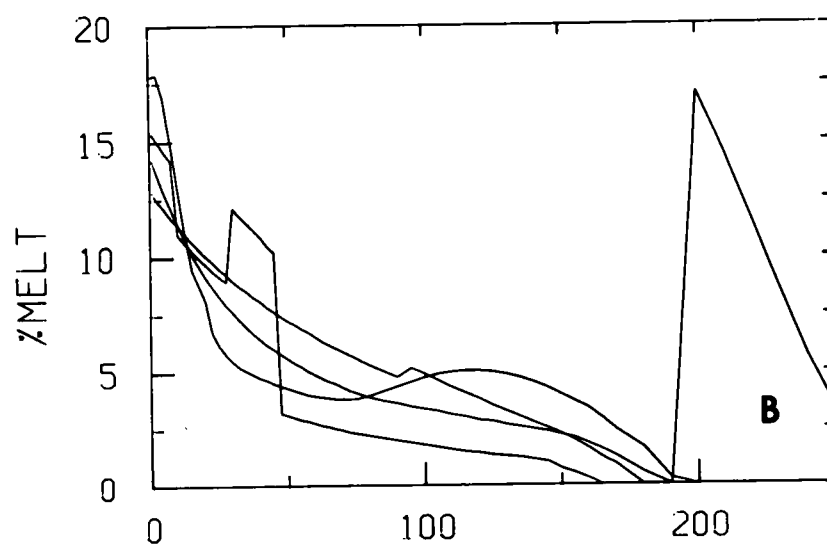
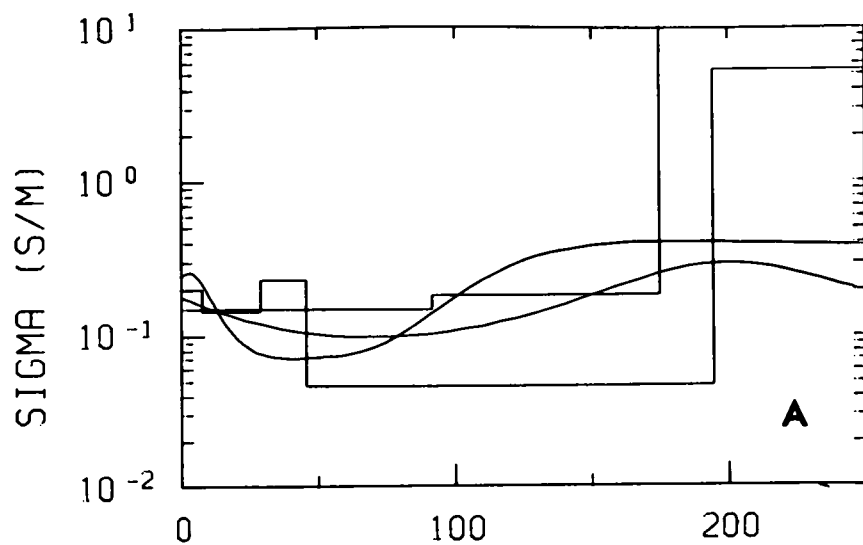
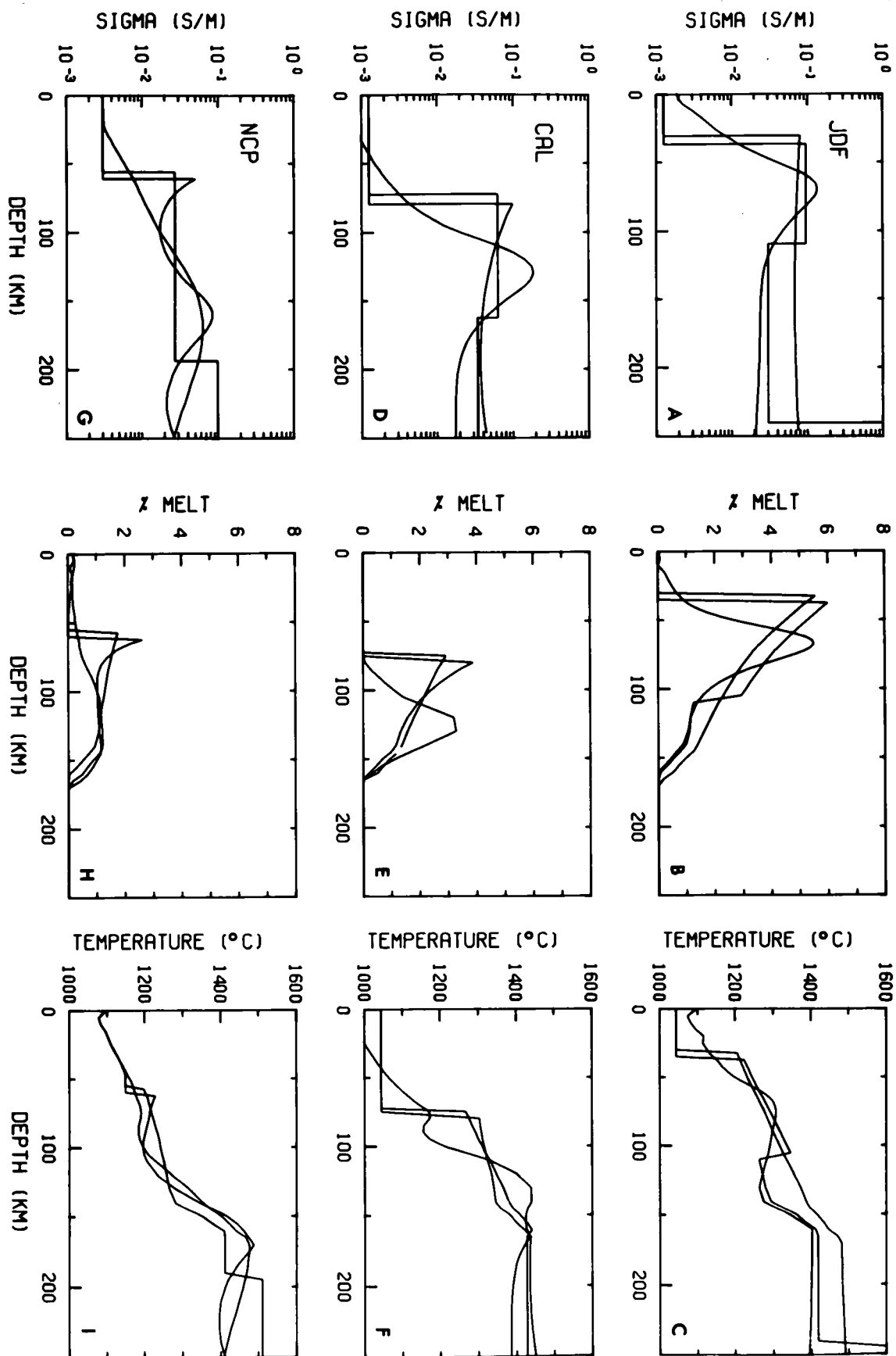


Figure 14.

Partial melting and temperature interpretations for the JDF data are given in the top row, panels A, B and C. The corresponding results for CAL are shown in the middle row, panels D, E and F. Results for NCP are shown in the bottom row, panels G, H and I.



f at 200 km but this is beyond the data resolution. the temperature curves in Figure 13C trend linearly from 1200°C near the surface to 1400°C at 120 km. The almost constant conductivity OBM models of Figure 13A generate quite featureless melt fraction and temperature profiles. In contrast, results from the other three sites, shown in Figure 14, are more structured. There, the varying conductivities produce melt fractions ≤ 5 percent within definite zones and temperature curves which are generally reduced from OBM levels.

A full geologic interpretation which draws together results from all four data sets is beyond the scope of this thesis. A coherent analysis of the three previous data sets has already been made by Oldenburg (1981). The discordant, high conductivities below the OBM site may be explained, in part, by the 7 km of conductive sediments ($\sigma=0.3$ to 1.0 S/m) in the region (L.K. Law, personal communication). One additional survey taken above 10 my lithosphere in August 1982 has yet to be analysed and may shift the interpretation balance to confirm the OBM site structure or certify it as anomalous. Hence, until this analysis is complete it is premature and perhaps unwise to go through great contortions to accomodate the apparently anomalous OBM results.

5.2 Suggestions for Future Work

Ocean bottom measurements of the electric as well as the magnetic field obviate the major problems with this analysis. No longer is the once removed ratio R the quantity in demand

since the sea-floor impedance is calculated directly from $E(\omega)$ and $H(\omega)$. All of the approximations accompanying the vertical gradient method, such as 1-D structure and the transport of VIC to above OBM, are circumvented. Thus, one link in the chain of approximations and assumptions is deleted and we are closer to a direct measure of the earth's conductivity. Moreover, the impedance tensor rotation properties are available to distinguish between one, two and three dimensional earth structures enabling appropriate inversion algorithms to be selected. Complete five component (E_x, E_y, H_x, H_y, H_z) ocean bottom MT instruments exist and have been used successfully. Unfortunately, the one deployed for this experiment ended up a few days later on the Washington coast looking as if it had been mauled by a trawler.

Choosing a more 'normal' land station for replacement of sea-surface fields is advisable failing a successful deployment of a five component instrument. VIC is surrounded by a complex pattern of straits and inlets which must make its records somewhat anomalous. Other geomagnetic observatories located near the coast of Oregon, for example, may yield fewer spurious ratio estimates.

Long data series of perhaps two or three months are essential for many reasons. Such extended records considerably increase the available degrees of freedom. Stacking and smoothing then gives stable impedance values with smaller error bars. The estimates are not only stable statistically but physically as well since they are based on a wider range of source field polarizations and angles of approach. Such

accurate data is important since it limits the vast non-uniqueness of acceptable conductivity models. Long time series also have more chance of producing long period responses which pass the winnowing criteria and hence provide resolution down to several hundred kilometers.

The resolution provided by MT responses and the uniqueness of constructed models are acute problems. Interesting features present on one model are absent from another. It is critical to find a way of quantifying the resolution and inferring just what structure the data truly require. Parker (1982) provides an analytic method of finding the maximum depth which the data can resolve. Oldenburg (1983) calculates bounds on the conductance down to a certain depth or on the average conductivity within a particular region. A complete appraisal theory for non-linear inverse problems has yet to be unveiled.

If the impedances indicate a two or three dimensional structure then the interpretation should be made in terms of these types of models. The process is not so easy, however. Two dimensional inversion programmes exist, but the non-uniqueness must be even worse than the very considerable 1-D non-uniqueness. As for the 1-D case, some effort must be made to assess the variability of possible 2-D models.

One way to limit acceptable conductivity profiles is to incorporate results from other geophysical surveys. Structures delineated by the different methods help to constrain the possible earth models and define a most probable one. Gravity data could be used although it is a very non-unique technique

itself and the connection between density and conductivity is not precise. Deep seismic soundings down to the Moho and below could identify major geologic units which correlate with conductivity anomalies. Heat flow is linked with conductivity since large values of either arise from elevated temperatures. High heat flow measurements in the OBM area would reinforce the case for the interpreted high conductivities.

Finally, the natural source MT method suffers from an incomplete knowledge of the source mechanisms and the fields they generate. Many techniques must be used to ensure that the impedances are not calculated on the basis of pathological sources. Tests of the validity of the plane wave assumption still depend on simplified source models. Theoretical and practical work on artificial controlled sources for MT should provide a substantial improvement in measured impedances and a better understanding of the earth's electrical conductivity.

REFERENCES

Backus, G. and Gilbert, F., 1970. Uniqueness in the inversion of inaccurate gross earth data, Trans. Phil. Roy. Soc., A266, 123-192.

Bailey, R.C., 1970. Inversion of the geomagnetic induction problem, Proc. Roy. Soc. London, A315, 185-194.

Banks, R.J., 1973. Data processing and interpretation in geomagnetic deep sounding, Phys. Earth Planet. Int., 7, 339-348.

Bendat, J.S. and Piersol, A.G., 1971. Random data: analysis and measurement procedures, John Wiley and Sons, New York.

Cagniard, L., 1953. Basic theory of the magnetotelluric method of geophysical prospecting, Geophysics, 18, 605-635.

Chave, A.D., Von Herzen, R.P., Poehls, K.A. and Cox, C.S., 1981. Electromagnetic induction fields in the deep ocean northeast of Hawaii: implications for mantle conductivity and source fields, Geophys. J. R. Astr. Soc., 66, 379-406.

Cox, C.S., Filloux, J.H. and Larsen, J.C., 1970. Electromagnetic studies of ocean currents and electrical conductivity below the ocean floor, in The Sea, 4, 637-693, ed. A.E. Maxwell, John Wiley and Sons, New York.

Eggers, D.E., 1982. An eigenstate formulation of the magnetotelluric impedance tensor, *Geophysics*, 47, 1204-1214.

Everett, J.E. and Hyndman, R.D., 1967. Geomagnetic variations and electrical conductivity structure in southwestern Australia, *Phys. Earth Planet. Int.*, 1, 24-34.

Filloux, J.H., 1967. Oceanic electric currents, geomagnetic variations and the deep electrical conductivity structure of the ocean-continent transition of central California, Ph.D. thesis, University of California, San Diego.

Filloux, J.H., 1973. Techniques and instrumentation for study of natural electromagnetic induction at sea, *Phys. Earth Planet. Int.*, 7, 323-338.

Filloux, J.H., 1977. Ocean-floor magnetotelluric sounding over North Central Pacific, *Nature*, 269, 297-301.

Filloux, J.H., 1980. Magnetotelluric soundings over the northeast pacific may reveal spatial dependence of depth and conductance of the asthenosphere, *Earth Planet. Sci. Lett.*, 46, 244-252.

Fischer, G., 1975. Symmetry properties of the surface impedance tensor for structures with a vertical plane of symmetry, *Geophysics*, 40, 1046-1050.

Fischer, G. and Schnegg, P.A., 1980. The dispersion relations of the magnetotelluric response and their incidence on the inversion problem, *Geophys. J. R. Astr. Soc.*, 62, 661-673.

Fischer, G., Schnegg, P.A., Peguiron, M. and Le Quang, B.V., 1981. An analytic one-dimensional magnetotelluric inversion scheme, *Geophys. J. R. Astr. Soc.*, 67, 257-278.

Gel'fand, I.M. and Levitan, R.M., 1955. On the determination of a differential equation by its spectral function, *Am. Math. Soc. Trans. Ser. 2*, 1, 253-304.

Hermance, J.F. and Peltier, W.R., 1970. Magnetotelluric fields of a line current, *J. Geophys. Res.*, 75, 3351-3356.

Jenkins, G.M. and Watts, D.G., 1968. Spectral analysis and its applications, Holden-Day, San Francisco.

Kaufman, A.A. and Keller, G.V., 1981. The magnetotelluric sounding method, Elsevier Scientific Publishing, Amsterdam.

Keller, G.V. and Frischknecht, F.C., 1966. Electrical methods in geophysical prospecting, Pergamon Press, Oxford.

Larsen, J.C., 1968. Electric and magnetic fields induced by deep sea tides, *Geophys. J. R. Astr. Soc.*, 16, 47-70.

Larsen, J.C., 1973. An introduction to electromagnetic

induction in the ocean, *Phys. Earth Planet. Int.*, 7, 389-398.

Law, L.K. and Greenhouse, J.P., 1981. Geomagnetic variation sounding of the asthenosphere beneath the Juan de Fuca ridge, *J. Geophys. Res.*, 86, 967-978.

Loewenthal, D. and Landisman, M., 1973. Theory for magnetotelluric observations on the surface of a layered anisotropic halfspace, *Geophys. J. R. Astr. Soc.*, 35, 195-214.

Oldenburg, D.W., 1979. One-dimensional inversion of natural source magnetotelluric observations, *Geophysics*, 44, 1218-1244.

Oldenburg, D.W., 1981. Conductivity structure of oceanic upper mantle beneath the Pacific plate, *Geophys. J. R. Astr. Soc.*, 65, 359-394.

Oldenburg, D.W., 1983. Appraisal in linear and non-linear inverse problems, submitted to *J. Geophys. Res.*

Oldenburg, D.W., Scheuer, T. and Levy, S., 1982. Recovery of the acoustic impedance from reflection seismograms. Submitted to *Geophysics*.

Parker, R.L., 1980. The inverse problem of electromagnetic induction: Existence and construction of solutions based on incomplete data, *J. Geophys. Res.*, 85, 4421-4428.

Parker, R.L. and Whaler, K.A., 1981. Numerical methods for establishing solutions to the inverse problem of electromagnetic induction, *J. Geophys. Res.*, 86, 9574-9584.

Parker, R.L., 1982. The existence of a region inaccessible to magnetotelluric sounding, *Geophys. J. R. Astr. Soc.*, 68, 165-170.

Parker, R.L., Oldenburg, D.W. and Whittall, K.P., 1983. Inversion of ocean bottom magnetotelluric data: revisited, submitted to *Geophys. J. R. Astr. Soc.*

Pedersen, L.B., 1982. The magnetotelluric impedance tensor-its random and bias errors, *Geophys. Prosp.*, 30, 188-210.

Peltier, W.R. and Hermance, J.F., 1971. Magnetotelluric fields of a Gaussian electrojet, *Canadian J. Earth Sci.*, 8, 338-346.

Poehls, K.A. and Von Herzen, R.P., 1976. Electrical resistivity structure beneath the northwest Atlantic ocean, *Geophys. J. R. Astr. Soc.*, 47, 331-346.

Ringwood, A.E., 1975. Composition and petrology of the earth's mantle, McGraw-Hill, New York.

Schmucker, U., 1970. Anomalies of geomagnetic variations in the south-western United States, *Bull. Scripps Inst. Oceanography*, 13, 1-165.

Shankland, T.J. and Waff, H.S., 1977. Partial melting and electrical conductivity anomalies in the upper mantle, J. Geophys. Res., 82, 5409-5417.

Vozoff, K., 1972. The magnetotelluric method in the exploration of sedimentary basins, Geophysics, 37, 98-141.

Weidelt, P., 1972. The inverse problem of geomagnetic induction, Z. Geophys., 38, 257-289.